

# The $\text{C}(^3\text{P}) + \text{O}_2(^3\Sigma_g^-) \leftrightarrow \text{CO}_2 \leftrightarrow \text{CO}(^1\Sigma^+) + \text{O}(^1\text{D})/\text{O}(^3\text{P})$ Reaction: Thermal and Vibrational Relaxation Rates from 15 K to 20000 K

Juan Carlos San Vicente Veliz,<sup>†</sup> Debasish Koner,<sup>†</sup> Max Schwilk,<sup>†,¶</sup> Raymond J. Bemish,<sup>‡</sup> and Markus Meuwly<sup>\*,†,§</sup>

<sup>†</sup>*Department of Chemistry, University of Basel, Klingelbergstrasse 80, CH-4056 Basel, Switzerland*

<sup>‡</sup>*Air Force Research Laboratory, Space Vehicles Directorate, Kirtland AFB, New Mexico 87117, USA*

<sup>¶</sup>*University of Vienna, Faculty of Physics, 1090 Vienna, Austria*

<sup>§</sup>*Department of Chemistry, Brown University, RI, USA*

E-mail: m.meuwly@unibas.ch

March 12, 2021

## Abstract

Thermal rates for the  $\text{C}(^3\text{P}) + \text{O}_2(^3\Sigma_g^-) \leftrightarrow \text{CO}(^1\Sigma^+) + \text{O}(^1\text{D})/\text{O}(^3\text{P})$  reaction are investigated over a wide temperature range based on quasi classical trajectory (QCT) simulations on 3-dimensional, reactive potential energy surfaces (PESs) for the  $^1\text{A}'$ ,  $(2)^1\text{A}'$ ,  $^1\text{A}''$ ,  $^3\text{A}'$  and  $^3\text{A}''$  states. The forward rate matches measurements at 15 K to 295 K whereas the equilibrium constant determined from the forward and reverse rates are consistent with those derived from statistical mechanics at high temperature. Vibrational relaxation,  $\text{O} + \text{CO}(\nu = 1, 2) \rightarrow \text{O} + \text{CO}(\nu = 0)$ , is found to involve

both, non-reactive and reactive processes. The contact time required for vibrational relaxation to take place is  $\tau \geq 150$  fs for non-reacting and  $\tau \geq 330$  fs for reacting (oxygen atom exchange) trajectories and the two processes are shown to probe different parts of the global potential energy surface. In agreement with experiments, low collision energy reactions for the  $\text{C}(^3\text{P}) + \text{O}_2(^3\Sigma_g^-, v = 0) \rightarrow \text{CO}(^1\Sigma^+) + \text{O}(^1\text{D})$  lead to  $\text{CO}(^1\Sigma^+, v' = 17)$  with an onset at  $E_c \sim 0.15$  eV, dominated by the  $^1\text{A}'$  surface with contributions from the  $^3\text{A}'$  surface. Finally, the barrier for the  $\text{CO}_\text{A}(^1\Sigma^+) + \text{O}_\text{B}(^3\text{P}) \rightarrow \text{CO}_\text{B}(^1\Sigma^+) + \text{O}_\text{A}(^3\text{P})$  atom exchange reaction on the  $^3\text{A}'$  PES yields a barrier of  $\sim 7$  kcal/mol (0.300 eV), consistent with an experimentally reported value of 6.9 kcal/mol (0.299 eV).

## Introduction

Reactions involving carbon and oxygen atoms play important roles in combustion, hypersonic flow, and planetary atmospheres.<sup>1</sup> Among those, the thermal rates for the  $\text{C}(^3\text{P}) + \text{O}_2(^3\Sigma_g^-)$ ,  $\text{O}(^3\text{P}) + \text{CO}(^1\Sigma^+)$ , and  $\text{O}(^1\text{D}) + \text{CO}(^1\Sigma^+)$  reactions going through various electronic states of  $\text{CO}_2$  (see Figure 1) are particularly relevant. Similarly, the vibrational deactivation of  $\text{CO}(^1\Sigma^+)$  through collisions with  $\text{O}(^3\text{P})$  is a relevant pathway for relaxation and redistribution of energy in nonequilibrium flow.<sup>2</sup>

Several independent studies have determined thermal rates for the forward  $\text{C}(^3\text{P}) + \text{O}_2(^3\Sigma_g^-)$  reaction.<sup>3-5</sup> Using the CRESU (Cinétique de Réaction en Ecoulement Supersonique Uniforme) technique<sup>5</sup> the thermal rate from experiments between 15 and 295 K was measured. At 298 K the rate was  $4.8 \pm 0.5 \cdot 10^{-11} \text{cm}^3 \text{ molecule}^{-1} \text{ s}^{-1}$  which is within a factor of two to three of other, previous experiments.<sup>3,4,6,7</sup> In all three laval nozzle experiments it was found that the rate increases with decreasing temperature between 15 and 295 K.<sup>5,8,9</sup> The product detection techniques included vacuum ultraviolet laser-induced fluorescence,<sup>5,9</sup> and chemiluminescence.<sup>8</sup>

Shock tube experiments of the C+O<sub>2</sub> reactions were also carried out at higher temperatures (from 1500 to 4200 K) and reported a rate of  $k_f(T) = 1.2 \times 10^{14} \exp(-2010\text{K}/T) \text{ cm}^3 \text{ mol}^{-1} \text{ s}^{-1}$  (corresponding to  $1.9 \times 10^{-10} \exp(-2010\text{K}/T) \text{ cm}^3 \text{ molecule}^{-1} \text{ s}^{-1}$ ) with an overall uncertainty of  $\pm 50\%$  and a standard deviation for the activation energy of  $\pm 15\%$  and  $\pm 13\%$ , respectively.<sup>10</sup> Yet earlier emission spectra in a discharge flow found that the C(<sup>3</sup>P) + O<sub>2</sub>(<sup>3</sup>Σ<sub>g</sub><sup>-</sup>) reaction generates CO in high vibrationally excited states (up to  $v' = 17$ ) and that the transition state has the configuration COO rather than OCO.<sup>11</sup> Such a COO intermediate was also proposed from the interpretation of the C+O<sub>2</sub> reaction<sup>12</sup> and has been described in multiconfiguration SCF calculations.<sup>13</sup> Also, no evidence was found that the C+O<sub>2</sub> reaction passes through the region where the quenching of O(<sup>1</sup>D) to O(<sup>3</sup>P) by CO occurs as a non-adiabatic process, as had been proposed earlier.<sup>14,15</sup>

For the reverse reactions, O(<sup>3</sup>P)+CO(<sup>1</sup>Σ<sup>+</sup>), and O(<sup>1</sup>D)+CO(<sup>1</sup>Σ<sup>+</sup>) leading to C(<sup>3</sup>P) + O<sub>2</sub>(<sup>3</sup>Σ<sub>g</sub><sup>-</sup>), the onset for the rates  $k_r(T)$  to form C+O<sub>2</sub> is expected to occur at considerably higher temperature than that for  $k_f$  due to the large energy difference of  $\sim 6$  eV between the O+CO and the C+O<sub>2</sub> asymptotes, see Figure 1. There are, however, computational investigations of the oxidation of CO to form CO<sub>2</sub> following the O(<sup>3</sup>P) + CO(<sup>1</sup>Σ<sup>+</sup>) → CO<sub>2</sub>(<sup>1</sup>Σ<sub>g</sub><sup>+</sup>) route, usually involving a third particle M.<sup>16</sup> The rates for formation of CO<sub>2</sub> along the <sup>3</sup>A' and <sup>3</sup>A'' pathways starting from O(<sup>3</sup>P)+CO(<sup>1</sup>Σ<sup>+</sup>) ranged from 10<sup>-13</sup> to 10<sup>-12</sup> cm<sup>3</sup> molecule<sup>-1</sup> s<sup>-1</sup>, depending on temperature, compared with  $\sim 10^{-14}$  cm<sup>3</sup> molecule<sup>-1</sup> s<sup>-1</sup> from earlier work.<sup>17</sup> These were non-Born-Oppenheimer dynamics simulations of the O(<sup>3</sup>P)+CO(<sup>1</sup>Σ<sup>+</sup>) → CO<sub>2</sub>(<sup>1</sup>Σ<sub>g</sub><sup>+</sup>) reaction involving the <sup>1</sup>A', <sup>3</sup>A', and <sup>3</sup>A'' potential energy surfaces (PESs).<sup>16</sup> The spin-forbidden fraction in this study was, however, found to be small ( $\sim 1\%$ ). Experimentally, the forward reaction has not been probed so far, to the best of our knowledge. Direct experiments involving [O(<sup>3</sup>P), O(<sup>1</sup>D))] and CO(<sup>1</sup>Σ<sup>+</sup>) concern the vibrational deactivation of CO upon collision with atomic oxygen.<sup>2,18-21</sup> Finally, the rate for collisional spin relaxation

for the  $O(^1D)$  to  $O(^3P)$  spin relaxation by  $CO(^1\Sigma^+)$  at temperatures between 113 and 333 K was determined.<sup>22</sup> The rates were found to vary monotonically from about  $7.6 \times 10^{-11}$  to  $5.2 \times 10^{-11} \text{ cm}^3 \text{ molecule}^{-1} \text{ s}^{-1}$  over the temperature range. Earlier modeling based on collisions with CO and other small molecules obtained a rate of  $8 \times 10^{-11} \text{ cm}^3 \text{ molecule}^{-1} \text{ s}^{-1}$ .<sup>23</sup>

Computationally, the ground and excited state PESs for  $CO_2$  have been studied in some detail.<sup>13,24-29</sup> Early configuration interaction calculations established<sup>24</sup> that there must be four states (two singlet and two triplet) of  $CO_2$  below the  $CO(^1\Sigma^+)+O(^3P)$  asymptote which is also what is found in the present work (Figure 1).  $CO_2$  does not show strong absorptions below 11 eV<sup>24</sup> which makes direct comparison difficult also, because often vertical and not adiabatic transition energies were measured. A low-lying adiabatic electronic transition to a triplet state was reported at  $39412 \text{ cm}^{-1}$  (4.89 eV) above the ground state,<sup>30</sup> in qualitative agreement with the position of the  $^3A'$  state, 4.62 eV above the ground state, see Figure 1.

An early classical MD study<sup>31</sup> of the forward reaction using an analytical potential energy surface found a rate of  $k_f = 1.92 \times 10^{-11} \text{ cm}^3 \text{ molecule}^{-1} \text{ s}^{-1}$ . In dynamics studies<sup>16,18,28,32,33</sup> the reference energies from electronic structure calculations were either represented as parametrized fits,<sup>18,32,33</sup> cubic splines,<sup>28</sup> or interpolated moving least squares.<sup>16</sup> Reference calculations were carried out at the CASSCF-MP2/631G+(d),<sup>18</sup> and MRCI+Q/aug-cc-pVQZ levels of theory.<sup>16,28,33</sup> The dynamics simulations either concerned the O-induced collisional dissociation of CO,<sup>33</sup> CO vibrational relaxation,<sup>18</sup> the O-exchange dynamics in reactive O+CO collisions, non-Born-Oppenheimer effects in  $CO_2$  formation from O+CO collisions,<sup>16</sup> or the final state distributions from the O+CO reactive scattering<sup>32</sup> but not the entire  $C(^3P) + O_2(^3\Sigma_g^-) \leftrightarrow CO_2 \leftrightarrow CO(^1\Sigma^+) + O(^1D)/O(^3P)$  reaction involving several electronic states.

A schematic of the states derived from the present calculations and considered in the present

work is provided in Figure 1. The left hand side is the  $C(^3P) + O_2(^3\Sigma_g^-)$  (entrance) channel which connects to all bound  $CO_2$  states in the middle. This asymptote is 11.22 eV above the global minimum which is the linear  $CO_2(^1A')$  structure. The right hand side of Figure 1 shows the two product channels considered: the lower  $CO(^1\Sigma^+) + O(^3P)$  state, 5.30 eV above the minimum energy of the  $CO_2(^1A')$  ground state, and the  $CO(^1\Sigma^+) + O(^1D)$  asymptote another 1.97 eV higher in energy. The final state involving  $O(^3P)$  connects with the triplet states ( $^3A'$  and  $^3A''$ ) of  $CO_2$  whereas that leading to  $O(^1D)$  correlates with the  $^1A'$ ,  $^1A''$ , and  $(2)^1A'$  states, see Figure 1.

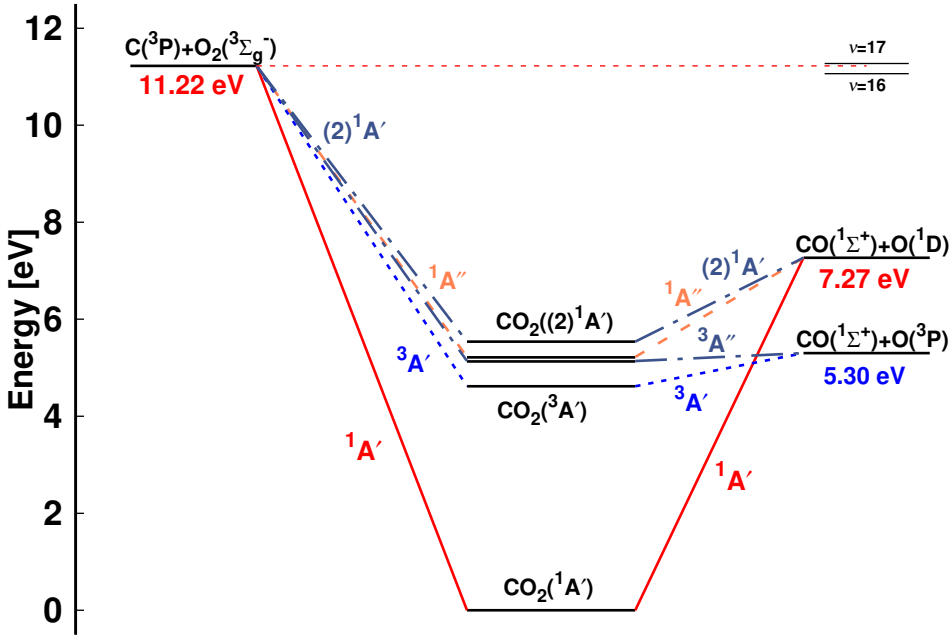


Figure 1: Energy level diagram for the  $C+O_2 \leftrightarrow CO+O$  reaction:  $C(^3P)+O_2(^3\Sigma_g^-) \leftrightarrow CO(^1\Sigma^+)+O(^3P)$  and  $C(^3P)+O_2(^3\Sigma_g^-) \leftrightarrow CO(^1\Sigma^+)+O(^1D)$ . The energies of the dissociating species are reported: the  $O(^1D)/O(^3P)$  separation is 1.97 eV, consistent with experiment, and the total energies for  $CO_2$  are  $^1A'$  ( $^1\Sigma_g$  in  $D_{\infty h}$ ) (0 eV),  $^3A'$  (4.62 eV),  $^3A''$  (5.14 eV),  $^1A''$  (5.22 eV), and  $(2)^1A'$  (5.53 eV). The relative positions of the  $CO(v' = 16)+O(^1D)$  and  $CO(v' = 17)+O(^1D)$  asymptotes, relevant for discussing the low energy collision  $C(^3P)+O_2(^3\Sigma_g^-) \leftrightarrow CO(^1\Sigma^+)+O(^1D)$  reaction,<sup>34</sup> are indicated on the right hand side. The correlation of the  $(2)^1A'$  state of  $CO_2$  based on state-averaged SA-CASSCF calculations given in Figure S1 with the reactant and product state is consistent with earlier work<sup>8</sup> but differs from others.<sup>13</sup>

Except for the shock tube experiments<sup>35</sup> on  $\text{C}+\text{O}_2 \rightarrow \text{O}+\text{CO}$  (1500-4200 K) and the computations<sup>16</sup> for  $\text{CO}_2$  formation from  $\text{O}+\text{CO}$  (between 1000 K and 5000 K) there is little information on the high-temperature dynamics of either, the  $\text{C}+\text{O}_2$  or the  $\text{O}+\text{CO}$  reactive processes. The present work extends this by performing QCT simulations on the 5 lowest states of  $\text{CO}_2$ , represented as a reproducing kernel Hilbert space (RKHS),<sup>36,37</sup> and focusing on the forward and reverse reactions and vibrational relaxation. First, the methods are presented and the potential energy surfaces for all 5 states are discussed. Then the thermal rates are determined along the singlet pathway. Next, vibrational relaxation for the  $\text{O}+\text{CO}$  collision is considered for  $\text{CO}(v = 1)$  and  $\text{CO}(v = 2)$  and the distributions for relaxing/nonrelaxing reactive/nonreactive trajectories are mapped onto the PES. Finally, conclusions are drawn.

## Computational Methods

This section presents the generation and representation of the potential energy surfaces and the methodologies for the QCT simulations and their analysis.

### Electronic Structure Calculations

All PESs are computed at the multi reference CI singles and doubles (MRCISD) level of theory<sup>38,39</sup> including the Davidson quadruples correction<sup>40</sup> (MRCISD+Q) together with the aug-cc-pVTZ basis set<sup>41</sup> using the MOLPRO 2019.1 software.<sup>42</sup> In order to consistently describe all relevant states and avoid numerical instabilities due to closely-lying states of the same symmetry, state-averaged CASSCF<sup>43-46</sup> calculations including the two lowest states of each symmetry (two spin symmetries and two spatial symmetries) were carried out. Hence, in total eight states are included in the CASSCF reference wave function. MRCI+Q calculations for both asymptotic channels followed for the 5 lowest  $\text{CO}_2$  states, namely  $^1\text{A}'$ ,  $^3\text{A}'$ ,

$^3A''$ ,  $^1A''$ , and  $(2)^1A'$ , see Figure 1.

The energies were computed on a grid defined by Jacobi coordinates  $(r, R, \theta)$  where  $r$  is the separation of the diatomic,  $R$  is the distance between the atom and the center of mass of the diatomic and  $\theta$  is the angle between the two unit vectors  $\vec{r}$  and  $\vec{R}$ . For channel I ( $C(^3P) + O_2(^3\Sigma_g^-)$ ) the  $R$ -grid included 28 points between 1.4 and 11  $a_0$  and the distance  $r$  was covered by 20 points between 1.55 and 4.10  $a_0$  whereas for channel II ( $O(^3P/^1D) + CO(^1\Sigma^+)$ ) the  $R$ -grid included 26 points between 1.8 and 11  $a_0$ , and the distance  $r$  was covered by 20 points between 1.55 and 4.00  $a_0$ . The angular grid for both channels contained 13 angles from a Gauss-Legendre quadrature ( $169.796^\circ$ ,  $156.577^\circ$ ,  $143.281^\circ$ ,  $129.967^\circ$ ,  $116.647^\circ$ ,  $103.324^\circ$ ,  $90.100^\circ$ ,  $76.676^\circ$ ,  $63.353^\circ$ ,  $50.033^\circ$ ,  $36.719^\circ$ ,  $23.423^\circ$ ,  $10.204^\circ$ ).

The reference points are then represented using reproducing kernel Hilbert space (RKHS) techniques.<sup>36,37,47</sup> The quality of the representation is further checked using energies from additional, off-grid geometries. The global, reactive 3D PES  $V(r_1, r_2, r_3)$  for an electronic state is constructed by summing the weighted individual PESs for each channel

$$V(r_1, r_2, r_3) = \sum_{j=1}^3 w_j(r_j) V_j(R, r_j, \theta), \quad (1)$$

using an exponential switching function with weights

$$w_i(r) = \frac{e^{-(r_i/\sigma_i)^2}}{\sum_{j=1}^3 e^{-(r_j/\sigma_j)^2}}. \quad (2)$$

Here,  $\sigma_i$  are switching function parameters for channels I and II. These parameters were optimized by a least squares fit and yielded values of (0.90, 1.00, 1.00)  $a_0$ , (1.10, 1.05, 1.05)  $a_0$ , (0.9, 1.00, 1.00)  $a_0$ , (0.85, 1.25, 1.25)  $a_0$  and (1.05, 1.00, 1.00)  $a_0$  for the  $^1A'$ ,  $(2)^1A'$ ,  $^1A''$ ,  $^3A'$ , and  $^3A''$  PESs, respectively.

The - global and local - minima and transition states between the minima and/or entrance channels supported by the PESs were determined using BFGS minimization and the nudged elastic band method<sup>48</sup> as implemented in the atomic simulation environment (ASE).<sup>49</sup>

## Quasi-Classical Trajectory Simulations

The QCT simulations used in the present work have been extensively described in the literature.<sup>50-53</sup> Here, Hamilton’s equations of motion are solved using a fourth-order Runge-Kutta method. The time step was  $\Delta t = 0.05$  fs which guarantees conservation of the total energy and angular momentum. Initial conditions for the trajectories are sampled using standard Monte Carlo methods.<sup>50</sup> The reactant and product ro-vibrational states are determined following semiclassical quantization with quantum bound state calculations for the two diatomics. Since the ro-vibrational states of the product diatom are continuous numbers, the states need to be assigned to integer values for which a Gaussian binning (GB) scheme was used. For this, Gaussian weights centered around the integer values with a full width at half maximum of 0.1 were used.<sup>52,54,55</sup> It is noted that using histogram binning (HB) was found to give comparable results for a similar system.<sup>53</sup>

The thermal rate for an electronic state ( $i$ ) at a given temperature ( $T$ ) is then obtained from

$$k_i(T) = g_i(T) \sqrt{\frac{8k_B T}{\pi \mu}} \pi b_{\max}^2 \frac{N_r}{N_{\text{tot}}}, \quad (3)$$

where  $g_i(T)$  is the electronic degeneracy factor of state ‘ $i$ ’,  $\mu$  is the reduced mass of the collision system,  $k_B$  is the Boltzmann constant, and, depending on the specific process considered,  $N_r$  is the number of reactive or vibrationally relaxed trajectories. In the rate coefficient calculations, the initial ro-vibrational states and relative translational energy (collision energy  $E_c$ ) of the reactants for the trajectories are sampled from Boltzmann and Maxwell-Boltzmann



distributions at given  $T$ , respectively. The sampling methodology is discussed in detail in Ref.<sup>53</sup>

For the forward  $\text{C}(^3\text{P}) + \text{O}_2(^3\Sigma_g^-) \rightarrow \text{CO}(^1\Sigma^+) + \text{O}(^1\text{D})$  and reverse reactions  $\text{CO}(^1\Sigma^+) + \text{O}(^1\text{D}) \rightarrow \text{C}(^3\text{P}) + \text{O}_2(^3\Sigma_g^-)$  with rates  $k_f(T)$  and  $k_r(T)$ , respectively, the degeneracy factor is

$$g(^{1A'},(2)^{1A'},^{1A''})(T) = \frac{1}{(1 + 3 \cdot e^{-\frac{23.6}{T}} + 5 \cdot e^{-\frac{62.4}{T}})} \quad (4)$$

where the terms are the degeneracies of the  $J$  states for which the energy differences between the ground and the excited states are  $-23.6$  K and  $-62.4$  K, respectively. For the reactions leading to  $\text{O}(^3\text{P})$  and going through triplet  $\text{CO}_2$  the degeneracies are  $g(^{3A'},^{3A''}) = \frac{1}{3}$ . From  $k_f(T)$  and  $k_r(T)$  the equilibrium constant

$$K_{\text{eq}}(T) = \frac{k_f(T)}{k_r(T)}. \quad (5)$$

is determined.

## Results and Discussion

### The Potential Energy Surfaces

Two-dimensional contour plots of the PESs are shown in Figure 2 and the positions and relative energies of the critical points are summarized in Table 1. The left hand column in Figure 2 reports the PESs for the  $\text{C}+\text{O}_2$  asymptote whereas the right hand column that for the  $\text{CO}+\text{O}$  channel, including the linear ground state structure for  $\text{CO}_2$  (Figure 2b). All PESs for the  $\text{C}+\text{O}_2$  asymptote are manifestly symmetric with respect to  $\theta = 90^\circ$  with moderate anisotropies for the  $^1A'$  and  $^3A'$  states and increased anisotropies for all other PESs. Conversely, all PESs for the  $\text{O}+\text{CO}$  channel are single-minima PESs with their minima around  $140^\circ$ , except for the  $^1A'$  state which has a minima for the  $\text{OCO}$  ( $180^\circ$ ) and

OOO ( $0^\circ$ ) structures, see also Figure S2. The energy of the OOO state is 170.0 kcal/mol (7.37 eV) above the OCO minimum and the barrier height for transition between the OOO and OCO minima is 8.5 kcal/mol (0.369 eV). In addition, the existence of the local OOO minimum was confirmed at the MRCI+Q and CCSD(T) levels of theory and was suggested earlier from experiments<sup>11,12</sup> and calculations.<sup>13</sup>

The quality of the RKHS representations is reported in Figure S3. All root mean squared errors for both, on-grid and off-grid points are below 1 kcal/mol (0.043 eV), except for the  $^1A''$  PES for which it is 1.04 kcal/mol (0.045 eV), all evaluated on the mixed PESs, see Eqs. 1 and 2. For the individual channels the performance of the RKHS is even better. One dimensional cuts for an OCO angle of  $120^\circ$  directly comparing the reference points and the RKHS are shown in Figure S4 for the lowest five states. Importantly, for off-grid points which were not used to construct the PESs but to independently validate the RKHS representations, the RMSEs are all below 1 kcal/mol (0.043 eV), too.

For a better understanding of the shapes of the PESs, the SA-CASSCF/aug-cc-pVTZ wave functions were analyzed in more detail for the different states at a bent geometry ( $\theta = 117.65^\circ$ ), see Figure 3, for  $r_{\text{CO}} = 2.14 a_0$  and varying  $R$ . Figure 3A shows the valence molecular orbitals that are relevant for the description of the eight states in the SA-CASSCF calculations along the  $\text{CO}_2 \rightarrow \text{CO} + \text{O}$  dissociation for this bent geometry. Figure 3B depicts the dominant configuration state functions along this dissociation path. All states except for the energetically high lying  $(2)^3A'$  state resolve with one dominant CASSCF configuration state function for the eight computed states of SA-CASSCF and keep their characteristic configuration along the entire dissociation path. Hence, no avoided crossing of two states with the same symmetry is observed. Figure 3C shows the relative energetics (taking the  $\text{C}(^3\text{P}) + \text{O}(^3\text{P}) + \text{O}(^3\text{P})$  ground state computed with the same level of theory as the reference).

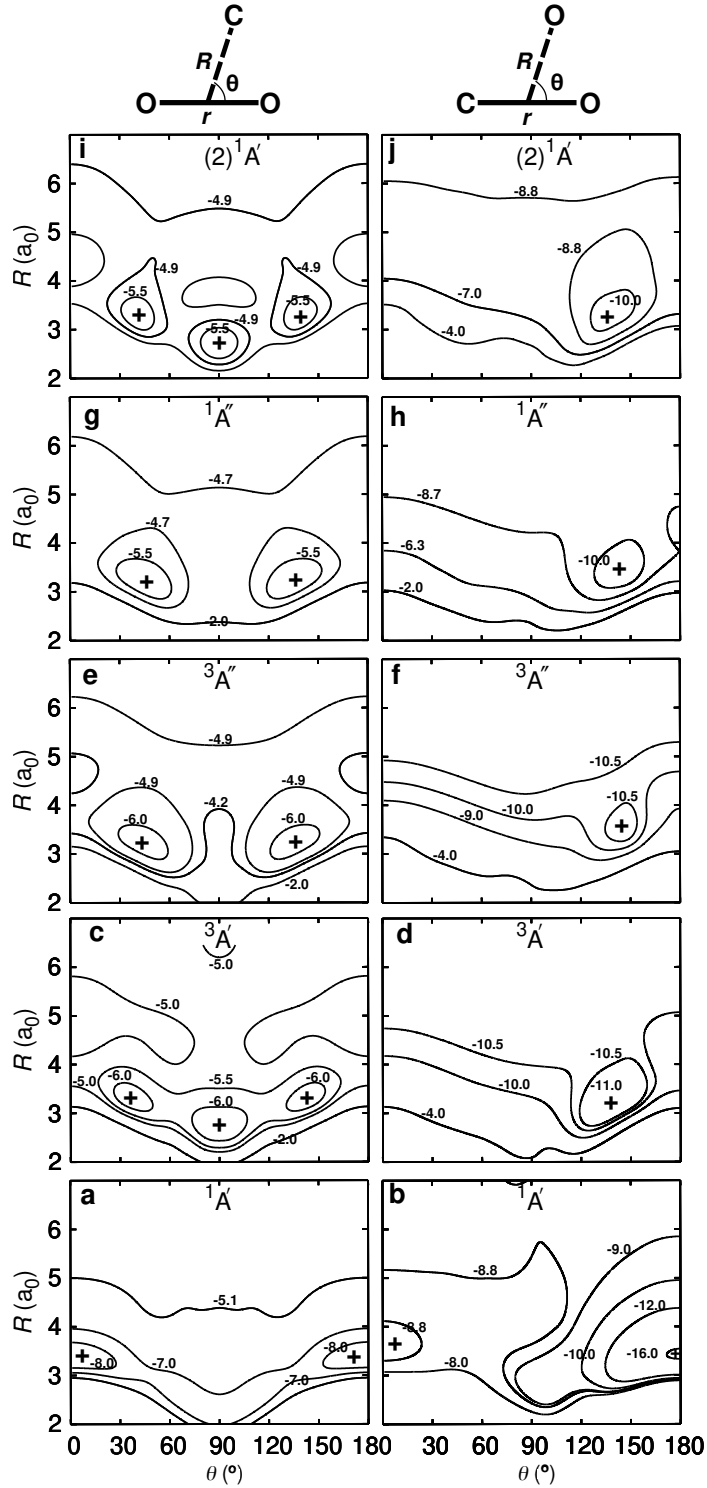


Figure 2: Two-dimensional cuts through the 3-d PES for the OO+C (left) and the CO+O (right) channels. Energy contours (in eV) for the  $1A'$  (panels a,b),  $3A'$  (panels c,d),  $3A''$  (panels e,f),  $1A''$  (panels g,h), and  $(2)1A'$  (panels i,j) states. The OO and CO diatomic distance are fixed at  $r = 2.14$  and  $r = 2.29 a_0$  for the CO+O and OO+C channels, respectively. The zero of energy is the dissociation into atomic fragments ( $C(3P) + O(3P) + O(3P)$ ). The symbol (“+”) indicates local and global minima on each PES.

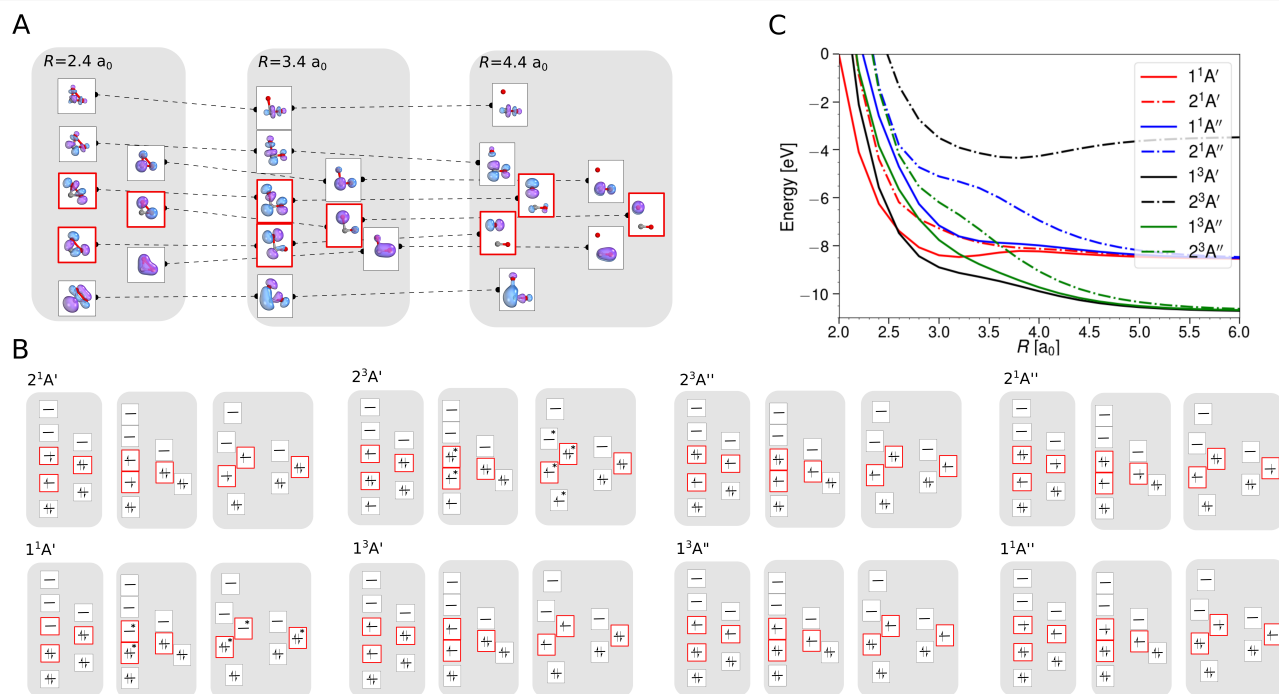


Figure 3: Analysis of the all-valence active space SA-CASSCF/aug-cc-pVTZ wave functions for a bent geometry with  $\theta = 117.65^\circ$ ,  $r_{\text{CO}} = 2.14$   $a_0$  and for  $R = 2.4, 3.4, 4.4$   $a_0$  ( $\text{CO}_2 \rightarrow \text{CO} + \text{O}$  dissociation path). A: Valence molecular orbitals (natural orbitals) energetically close to the three frontier orbitals (red frames) whose occupation defines the five lowest lying electronic states considered for the dynamics on the  $\text{CO}_2$  PES. The three depicted geometries are oriented with the symmetry plane parallel to the paper plane. Orbitals symmetric and antisymmetric with respect to the plane in the left and right columns of each diagram, respectively. B: Dominant configuration state functions of the eight states included in the SA-CASSCF calculation depicted as MO diagrams of the orbitals presented in panel A. If other configurations contributed with a weight  $> 0.05$ , the orbitals involved in the entanglement are marked by an asterisk (i. e. these orbitals have an occupation number that deviates significantly from the depicted integer value). C: Energy curves of the eight states for the  $\text{CO}_2 \rightarrow \text{CO} + \text{O}$  dissociation at this bent geometry. The ground state  $\text{C} + \text{O} + \text{O}$  energy computed at the same level of theory is the reference energy.

Table 1: Minima (MIN $i$ ) and transition states (TS $i$ ) on the CO<sub>2</sub> PESs towards the CO(<sup>1</sup>Σ<sup>+</sup>) + O(<sup>3</sup>P) asymptote using the Nudged Elastic Band (NEB) method.<sup>48</sup> The PESs are in ascending energetic order, see Figure 2. Distances are in a<sub>0</sub> and Energy in eV. Energies relative to the CO(<sup>1</sup>Σ<sup>+</sup>) + O(<sup>3</sup>P) dissociation limit. Present values are compared with previous work: for triplet states top row Ref.,<sup>16</sup> bottom row Ref.<sup>18</sup> For the global minimum in the <sup>1</sup>A' state: top row experiment,<sup>56</sup> bottom row Ref.<sup>16</sup> and for the remaining minima and transition states Ref.<sup>57</sup> Where necessary, literature values were converted to a<sub>0</sub> and eV.

PES	Present Work				Literature <sup>16,18,56-58</sup>			
	$r_1(\text{CO}_A)$	$r_2(\text{CO}_B)$	$\angle(\text{OCO})$	$E$ (eV)	$r_1$	$r_2$	$\angle(\text{OCO})$	$E$ (eV)
(2) <sup>1</sup> A' MIN	2.368	2.368	119.0	0.23	–	–	–	–
<sup>1</sup> A'' MIN	2.374	2.374	130.5	-0.13	–	–	–	–
<sup>3</sup> A'' MIN	2.374	2.374	130.6	-0.14	2.364	2.364	127.2	-0.23
					2.399	2.399	127.0	-0.22
<sup>3</sup> A'' TS	2.165	3.431	135.8	0.47	2.147	3.515	126.2	0.35
					2.192	3.496	122.0	0.30
<sup>3</sup> A' MIN	2.356	2.356	126.3	-0.69	2.381	2.381	118.0	-0.94
					2.349	2.349	118.0	-0.92
<sup>3</sup> A' TS	2.163	3.544	116.3	0.39	2.143	3.628	120.8	0.28
					2.192	3.779	112.0	0.20
<sup>1</sup> A' (Global-M)	2.206	2.206	180.0	-5.30	2.196	2.196	180.0	-5.45
					2.194	2.194	180.0	-5.64
<sup>1</sup> A' (MIN1)	2.527	2.527	70.6	0.74	2.522	2.522	72.9	0.61
<sup>1</sup> A' (MIN2)	2.192	4.798	0.0	1.88	2.220	4.716	0.0	1.72
<sup>1</sup> A' (TS1)	2.502	2.430	88.4	1.05	2.600	2.309	91.8	1.04
<sup>1</sup> A' (TS2)	2.164	4.279	68.9	2.15	2.203	4.537	41.0	2.22

Upon bending, the doubly degenerate  $\pi_3$  non-bonding [doubly occupied in <sup>1</sup>A'], as well as the  $\pi_3$  antibonding [unoccupied in <sup>1</sup>A'] orbitals for collinear CO<sub>2</sub> undergo a splitting due to the lifted degeneracy. This results in a Jahn-Teller splitting of the states <sup>1</sup>A'', <sup>3</sup>A'', <sup>3</sup>A', and (2)<sup>1</sup>A' of CO<sub>2</sub> with their energy minimum at a bent geometry, see right hand column in Figure 2. The splitting of the degenerate HOMO and LUMO  $\pi_3$  orbitals upon bending leads to three frontier orbitals, similar in energy, and with overall occupation of four electrons in all five energetically low-lying states (red frames in Figure 3A). One of these three frontier orbitals has  $\sigma^*$  character along the O-O bond (see Figure 3A) and is somewhat higher in energy. States that involve double occupation of this orbital lie higher in energy. Along the same line, states that involve single occupation of one of the strongly bonding orbitals below the frontier orbitals also lie energetically higher.

The  ${}^3A'$  and  ${}^3A''$  states are lower in energy than the  ${}^1A'$  state for certain bent geometries (see Figures 2 and 3C), as the triplet states gain from increased Pauli exchange, as well as reduced Coulomb repulsion due to the single occupations of orbitals. The corresponding open shell singlet states [ $(2){}^1A'$  and  ${}^1A''$ ] lie slightly higher in energy than their triplet counterparts due to reduced Pauli exchange.

All  $\text{CO}_2$  singlet states connect to  $\text{CO}({}^1\Sigma^+)+\text{O}({}^1\text{D})$  upon dissociation whereas the  ${}^3A'$ ,  ${}^3A''$ , and  $(2){}^3A''$  states connect to the  $\text{CO}({}^1\Sigma^+)+\text{O}({}^3\text{P})$  state. On the other hand, the  $(2){}^3A'$  connects to the energetically high-lying excited  $\text{CO}({}^3\Pi)+\text{O}({}^3\text{P})$  state. The low-lying triplet  $\text{CO}_2$  states have no or rather low barriers towards their dissociation across the entire PES (see Figure 2 and Figure 3C). Specifically, the  $(2){}^3A''$  state connects to the ground state of  $\text{CO} + \text{O}$  and crosses the singlet states upon dissociation. The crossing should nevertheless only lead to negligible non-adiabatic transition rates, as they are spin-forbidden. Since this state involves double occupation of an orbital with  $\sigma^*$  character of the O-O bond, it correlates with high lying excited states in the  $\text{C} + \text{O}_2$  channel and is energetically well separated from the  ${}^3A''$  state whenever there are short O-O distances. It is therefore sufficient to take its occupation only into account via the degeneracy of  $\text{O}({}^3\text{P})$  in the quasi-classical treatment of the  $\text{CO} + \text{O}$  dissociation channel.

## Forward and Reverse Rates and the Equilibrium Constants

*The forward reaction*  $\text{C}({}^3\text{P}) + \text{O}_2({}^3\Sigma_g^-)$  (Figure 1) generates ground and excited state oxygen ( ${}^3\text{P}$  and  ${}^1\text{D}$ ). The pathway to yield  ${}^3\text{P}$  involves the  ${}^3A'$  and  ${}^3A''$   $\text{CO}_2$  PESs whereas that to form  ${}^1\text{D}$  goes through the  ${}^1A'$ ,  $(2){}^1A'$ , and  ${}^1A''$  states. For each of the reactions on each PES a minimum of  $5 \times 10^5$  trajectories was run at each temperature.

Figure 4 shows the total thermal rates for formation of O(<sup>1</sup>D) and O(<sup>3</sup>P). The rates for formation of O(<sup>1</sup>D) start at  $1.72 \times 10^{-10} \text{ cm}^3 \text{ molecule}^{-1} \text{ s}^{-1}$  at 15 K, drop to  $5.19 \times 10^{-11} \text{ cm}^3 \text{ molecule}^{-1} \text{ s}^{-1}$  for  $T \sim 600 \text{ K}$  and then monotonically increase to  $3.23 \times 10^{-10} \text{ cm}^3 \text{ molecule}^{-1} \text{ s}^{-1}$  for higher temperatures, see red line for the total rate in Figure 4 with explicit numerical values reported in Table S1 which also reports the number of reactive trajectories that contribute to the rate. Experimentally, the total rate for this process was determined over the temperature range from 1500 K to 4000 K.<sup>35</sup> Evaluating the reported expression  $k(T) = 1.2 \times 10^{14} e^{-\frac{2010\text{K}}{T}} (\pm 50\%) \text{ cm}^3 \text{ molecule}^{-1} \text{ s}^{-1}$  at 1500 K and 4000 K yields rates of  $k(1500) = 5.22 \times 10^{-11} \text{ cm}^3 \text{ molecule}^{-1} \text{ s}^{-1}$  and  $k(4000) = 1.21 \times 10^{-10} \text{ cm}^3 \text{ molecule}^{-1} \text{ s}^{-1}$ . This compares with  $k(1500) = 5.96 \times 10^{-11} \text{ cm}^3 \text{ molecule}^{-1} \text{ s}^{-1}$  and  $k(4000) = 1.05 \times 10^{-10} \text{ cm}^3 \text{ molecule}^{-1} \text{ s}^{-1}$ , respectively, from the present simulations. A high temperature measurement at 8000 K, associated with a substantial uncertainty, yields  $k \sim 5 \times 10^{-10} \text{ cm}^3 \text{ molecule}^{-1} \text{ s}^{-1}$ .<sup>59</sup>

The inset of Figure 4 reports the low-temperature results. Starting at 15 K the rate first decreases, goes through a minimum (at  $\sim 600 \text{ K}$ ) before it raises again for higher temperatures. Such a behaviour is indicative of a submerged barrier<sup>62</sup> which, based on the rates for individual surfaces, appears to be dominated by the <sup>1</sup>A' and <sup>3</sup>A' states, as seen in Figure S5. Compared with experiments all computed rates are within 2 % to 20 % at 50 K and 30 % to 40 % for Ref.<sup>9</sup> and 4 % to 30 % at 300 K for Ref.<sup>5</sup> which can be considered good agreement. For the process to yield O(<sup>3</sup>P) the individual rates from the contribution of both triplet PESs (<sup>3</sup>A' and <sup>3</sup>A'') as well as the total weighted sum from the process to yield O(<sup>1</sup>D) and O(<sup>3</sup>P) are also reported in Figure 4 (blue and black lines), with numerical values given in Table S2.

*For the reverse reaction,  $\text{CO}({}^1\Sigma^+) + \text{O}({}^1\text{D})/\text{O}({}^3\text{P}) \rightarrow \text{C}({}^3\text{P}) + \text{O}_2({}^3\Sigma_g^-)$ , similar simulations were carried out. As this is an uphill process (Figure 1), this channel only opens at higher*

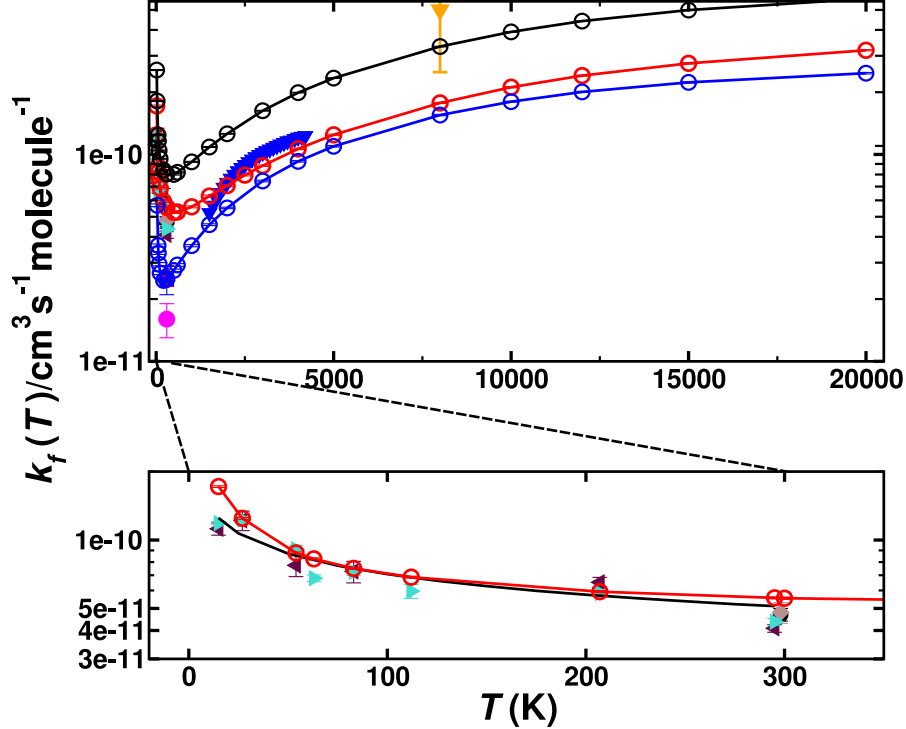


Figure 4: Thermal rate for the forward reaction ( $k_f$ )  $\text{C}(^3\text{P}) + \text{O}_2(^3\Sigma_g^-) \rightarrow \text{CO}(^1\Sigma^+) + \text{O}(^1\text{D})/\text{O}(^3\text{P})$ . The sum of the contribution of the singlet (red circles) and triplet (blue circles) states and the total rate (black circles). Comparison with forward rates from experiments: Ref.<sup>35</sup> (solid blue triangles) Ref.<sup>8</sup> (solid green right triangle), Ref.<sup>7</sup> (solid magenta circle), Ref.<sup>6</sup> (solid black circle),<sup>60</sup> (solid blue square), Ref.<sup>5</sup> (grey diamond), Ref.<sup>59</sup> (solid orange triangle down) and Ref.<sup>61</sup> (red triangle). The bottom panel shows an enlarged view for  $0 < T < 300$  K for the total singlet rate (solid red line) together with the experimental results and a fit using Arrhenius parameters provided in the literature<sup>5</sup> (inset, black solid line).

temperature, see Figure 5. The dynamics for  $\text{CO}(^1\Sigma^+) + \text{O}(^1\text{D}) \rightarrow \text{C}(^3\text{P}) + \text{O}_2(^3\Sigma_g^-)$  involves the  $^1A'$ ,  $(2)^1A'$ , and  $^1A''$  states (for numerical values see Table S3), whereas that for  $\text{CO}(^1\Sigma^+) + \text{O}(^3\text{P}) \rightarrow \text{C}(^3\text{P}) + \text{O}_2(^3\Sigma_g^-)$  is related to the  $^3A'$  and  $^3A''$  states, given in Table S4. Compared with the forward rates, those for the reverse reaction are typically 1 to 5 orders of magnitude smaller. The reverse rates starting from  $\text{O}(^1\text{D})$  are larger by 1 to 2 orders of magnitude at high  $T$  than those from  $\text{O}(^3\text{P})$  which is consistent with the Boltzmann-weighted energy difference for the two asymptotes.



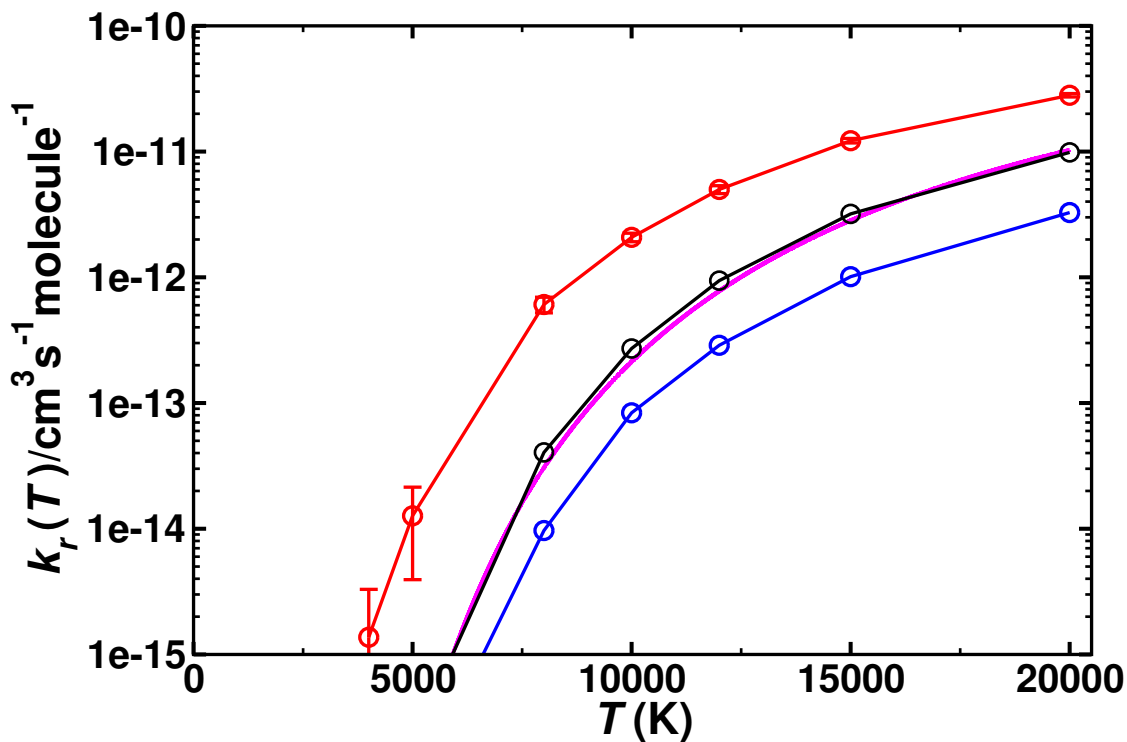


Figure 5: Thermal rate for the reverse ( $k_r$ ) reaction  $\text{CO}(^1\Sigma^+) + \text{O}(^1\text{D}) \rightarrow \text{C}(^3\text{P}) + \text{O}_2(^3\Sigma_g^-)$ . The sum of the contributions of the singlet (red circles, with error bars from bootstrapping) and triplet (blue circles) states and their Boltzmann-weighted sum (black circles). The temperature range is from 5000-20000 K. Comparison with recent theoretical work<sup>33</sup> (magenta solid line).

Table 2 summarizes the parameters from fitting the raw data to a modified Arrhenius expression  $k(T) = AT^n \exp(-\epsilon/T)$  for the forward and reverse processes for all five PESs. It is noted that all forward processes involve a comparatively small activation energy  $\epsilon$  of a few hundred to a few thousand Kelvin. All reverse rates have activation energies that are at least one order of magnitude larger. The number of trajectories that contribute to these rates varies from less than 1 % to 55 %. For the slowest process, the reverse reaction on the  $^3\text{A}'$  and  $^3\text{A}''$  PESs originating from  $\text{O}(^3\text{P})$ , at least an additional  $5 \times 10^5$  trajectories were run at each temperature between 3000 K and 20000 K and close to  $10^6$  trajectories for  $T \leq 1000$  K.

From the forward and reverse rates the equilibrium constant  $K_{\text{eq}}(T)$  can also be determined,

Table 2: Modified Arrhenius 3-parameter model for the forward  $\text{C}(^3\text{P}) + \text{O}_2(^3\Sigma_g^-) \rightarrow \text{CO}(^1\Sigma^+) + \text{O}(^1\text{D})/\text{O}(^3\text{P})$  and reverse  $\text{O}(^1\text{D})/\text{O}(^3\text{P}) + \text{CO}(^1\Sigma^+) \rightarrow \text{C}(^3\text{P}) + \text{O}_2(^3\Sigma_g^-)$  reaction.  $A$  in units of  $\text{cm}^3 \text{ s}^{-1} \text{ molecule}^{-1}$  and  $\epsilon$  in Kelvin. The temperature range for the modified Arrhenius fit is 5000 to 20000 K.

Forward	$A$	$n$	$\epsilon$
$\text{C}(^3\text{P}) + \text{O}_2(^3\Sigma_g^-) \rightarrow \text{CO}(^1\Sigma^+) + \text{O}(^1\text{D})$	$4.12 \times 10^{-12}$	0.45	2209
$^1\text{A}'$	$2.42 \times 10^{-12}$	0.40	116
$(2)^1\text{A}'$	$1.21 \times 10^{-12}$	0.47	4506
$^1\text{A}''$	$1.06 \times 10^{-11}$	0.27	6639
$\text{C}(^3\text{P}) + \text{O}_2(^3\Sigma_g^-) \rightarrow \text{CO}(^1\Sigma^+) + \text{O}(^3\text{P})$	$3.50 \times 10^{-11}$	0.22	3513
$^3\text{A}'$	$1.60 \times 10^{-11}$	0.22	1891
$^3\text{A}''$	$5.49 \times 10^{-11}$	0.11	6789
Total	$1.56 \times 10^{-11}$	0.30	3018
Reverse			
$\text{O}(^1\text{D}) + \text{CO}(^1\Sigma^+) \rightarrow \text{C}(^3\text{P}) + \text{O}_2(^3\Sigma_g^-)$	$1.15 \times 10^{-10}$	0.11	49965
$^1\text{A}'$	$1.25 \times 10^{-12}$	0.42	42273
$(2)^1\text{A}'$	$4.60 \times 10^{-12}$	0.32	50111
$^1\text{A}''$	$5.28 \times 10^{-13}$	0.53	46836
$\text{O}(^3\text{P}) + \text{CO}(^1\Sigma^+) \rightarrow \text{C}(^3\text{P}) + \text{O}_2(^3\Sigma_g^-)$	$1.52 \times 10^{-12}$	0.50	68903
$^3\text{A}'$	$8.92 \times 10^{-14}$	0.70	64167
$^3\text{A}''$	$7.80 \times 10^{-09}$	-0.37	83013
Total	$1.55 \times 10^{-10}$	0.09	71735

see Figure 6. This equilibrium constant was determined from the total forward and reverse fluxes of the weighted sum of the singlet and triplet pathways according to the data summarized in Table 2. Error bars for the individual rates have been determined from bootstrapping and are compared with results determined from statistical mechanics. The equilibrium constant is only reported for temperatures 5000 K and higher as the reverse reaction only opens at these temperatures, see Figure 5.

A final process considered is the atom exchange reaction  $\text{CO}_\text{A}(^1\Sigma^+) + \text{O}_\text{B}(^3\text{P}) \rightarrow \text{CO}_\text{B}(^1\Sigma^+) + \text{O}_\text{A}(^3\text{P})$ . For this process, on the  $^3\text{A}'$  state, rates ranging from  $5 \times 10^{-16} \text{ cm}^3 \text{ molecule}^{-1} \text{ s}^{-1}$  to  $6 \times 10^{-11} \text{ cm}^3 \text{ molecule}^{-1} \text{ s}^{-1}$  between 500 K and 20000 K were found, see Table S5 and Figure S6. The rate increases monotonically from values  $\sim 10^{-16}$ , consistent with those measured experimentally,<sup>64</sup> as a function of  $T$  and is smaller than the measurement at 1820

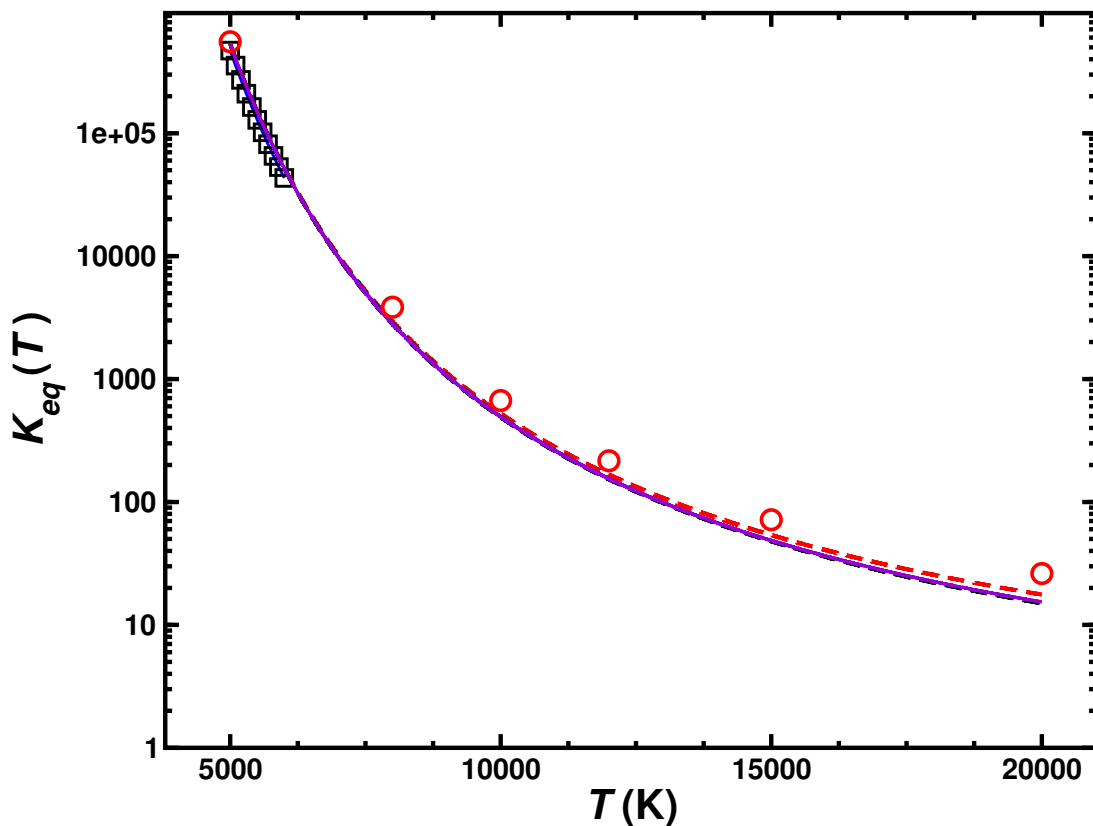


Figure 6: Equilibrium constant for the  $C(^3P) + O_2(^3\Sigma_g^-) \leftrightarrow CO(^1\Sigma^+) + O(^1D_1)$  ( $k_1$ ) and  $C(^3P) + O_2(^3\Sigma_g^-) \leftrightarrow CO(^1\Sigma^+) + O(^3P)$  ( $k_2$ ) reactions. The results from the JANNAF tables<sup>63</sup> (black open squares), those derived from equilibrium statistical mechanics ( $k_1$  (red open circles and red dashed line),  $k_2$  (black dashed line) and their Boltzmann-weighted total  $wk_1 + (1 - w)k_2$  (purple solid line)) with those from the QCT simulations are compared.

K.<sup>65</sup> This experimental value was an indirect measurement that required the decomposition rate for  $N_2O$  and is presented without derived error bars. The barrier for the atom exchange reaction inferred from the low-temperature experiments is 6.9 kcal/mol (0.299 eV), which is also what is found from the present work (Figures S7 and S8).

A summary of all forward and reverse rates is provided in Figure S5, and Tables S1 to S5 report all numerical values for the temperature dependent rates.

## Vibrational Relaxation

Vibrational relaxation (VR) of CO in its  $v = 1$  and  $v = 2$  states was investigated for both, the singlet and triplet manifolds separately. VR was investigated by running  $5 \times 10^5$  trajectories at each temperature, ranging from 300 K to 5000 K, see Table S6. The final vibrational state was determined using Gaussian binning (GB) which has been shown to yield similar results as histogram binning.<sup>54,55,66</sup> Figure 7 compares the individual and total VR rates with those measured experimentally and Table 3 reports the rates. The computed rates are consistently lower than those from experiments at lower temperatures. For  $T > 2000$  K the rates are in good agreement with experiments, though. In order to verify that the underestimation is not due to neglect of higher electronically excited states, the  $(2)^3A''$  PES was also determined. This PES (not shown) is mainly repulsive. Therefore, the VR rates for this state only contribute  $\sim 10\%$  of the rates for the  $^3A'$  and  $^3A''$  states at the highest temperatures. Hence, the differences between experiment and simulations at lower temperatures are not due to neglect of contributions from higher-lying electronic states.

Table 3: Vibrational relaxation rates (in units of  $10^{13}\text{cm}^3 \text{ molecule}^{-1} \text{ s}^{-1}$ )  $k_{\nu \rightarrow \nu'}$  for the collision of  $\text{O}(^3P)$  with  $\text{CO}(^1\Sigma_g)$ :  $\text{O}+\text{CO}(\nu = 1) \rightarrow \text{O}+\text{CO}(\nu' = 0)$  for the  $^3A'$ ,  $^3A''$ , and  $(2)^3A''$  states and the total contribution using GB.

	500 K	1000 K	2000 K	3000 K	4000 K	5000 K
$^3A'$	0.01	1.51	18.61	43.62	74.44	101.95
$^3A''$	0.01	1.08	14.90	39.70	67.00	99.30
$(2)^3A''$	0.00	0.07	1.90	4.71	7.83	11.73
Total	0.02	2.66	35.41	88.03	149.27	212.98

In order to better characterize to which parts of the PESs the individual processes are sensitive to, density maps were determined as follows. For each initial condition a trajectory can be attributed to one of the 4 possible outcomes: a) no vibrational relaxation, no reaction:  $\text{O}+\text{CO}(\nu = 1) \rightarrow \text{O}+\text{CO}(\nu' = 1)$  b) vibrational relaxation without reaction:  $\text{O}+\text{CO}(\nu = 1) \rightarrow \text{O}+\text{CO}(\nu' = 0)$ , c) no vibrational relaxation but with atom exchange:  $\text{O}_A+\text{CO}_B(\nu = 1) \rightarrow \text{O}_B+\text{CO}_A(\nu' = 1)$ , and d) vibrational relaxation with atom exchange:  $\text{O}_A+\text{CO}_B(\nu = 1) \rightarrow$

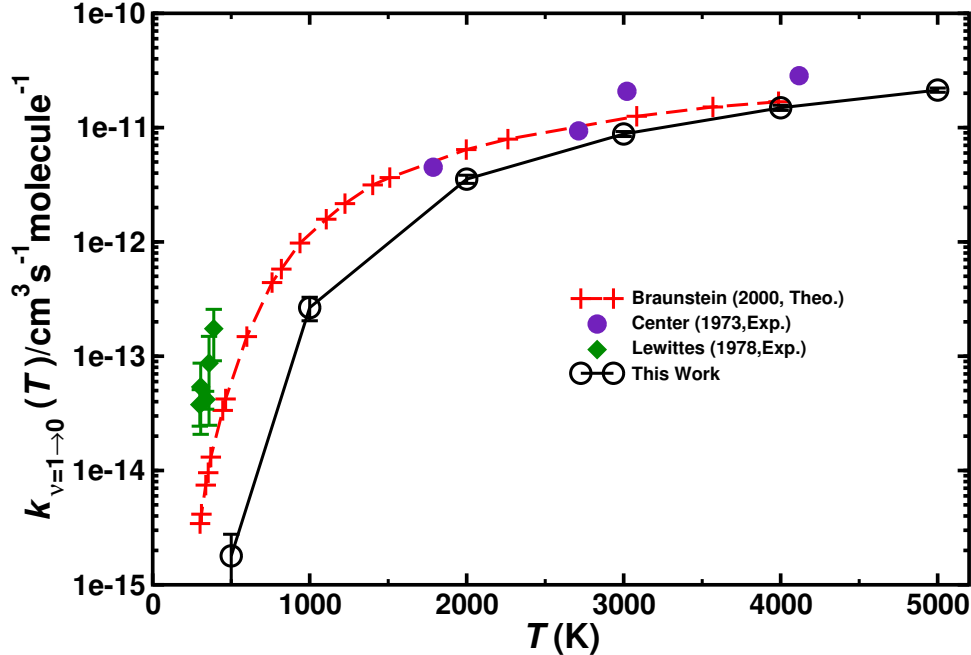


Figure 7: Total vibrational relaxation rate for  $\text{O}+\text{CO}(\nu = 1) \rightarrow \text{O}+\text{CO}(\nu = 0)$ . Total contribution ( ${}^3A'+{}^3A''$ ) (closed black circles) ( $g(e) = 1/3$ ). Literature values are the symbols as indicated.<sup>2,18,20</sup>  $5 \times 10^5$  trajectories were run at every temperature.

$\text{O}_B+\text{CO}_A(\nu' = 0)$ . Then, all trajectories for a given class were combined and a 2-dimensional histogram was generated and smoothed using kernel density estimation (KDE).<sup>67</sup> The resulting 2-dimensional distribution was then projected onto the relaxed PES for the corresponding state, see Figure 8.

Table 4: Average contact time ( $\tau_c$  in fs, for definition see text) and number  $N$  of trajectories for each final state for  $N_{\text{tot}} = 5 \times 10^5$  trajectories for each of the processes considered. In each case the difference ( $N_{\text{tot}} - N$ ) are fly-by trajectories. This table reports the cases  $\nu = 2 \rightarrow x$  and  $\nu = 1 \rightarrow x$  for both reactive and non-reactive events.

	relaxing			nonrelaxing	
reacting	$\nu = 2 \rightarrow 1$	$\nu = 2 \rightarrow 0$	$\nu = 1 \rightarrow 0$	$\nu = 2 \rightarrow 2$	$\nu = 1 \rightarrow 1$
$N$	300	230	681	340	745
$\tau_c$	210	207	333	241	301
non-reacting					
$N$	480	440	1579	65790	117367
$\tau_c$	67	155	156	33	36

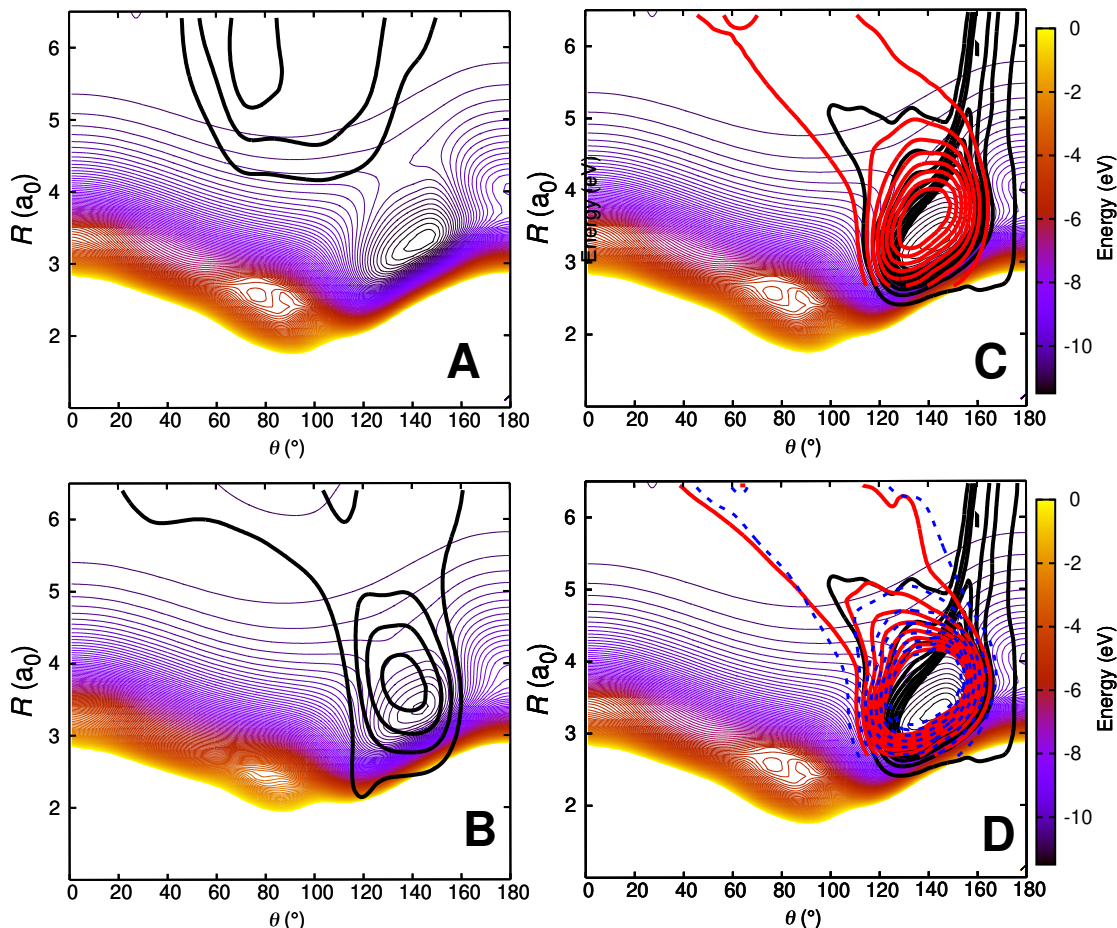


Figure 8: Density map for  $\text{O}+\text{CO}(\nu = 1)$  collisions at 1000 K on the relaxed  ${}^3\text{A}'$  PES. Panel A:  $\text{O}+\text{CO}(\nu = 1) \rightarrow \text{O}+\text{CO}(\nu' = 1)$ ; Panel B:  $\text{O}+\text{CO}(\nu = 1) \rightarrow \text{O}+\text{CO}(\nu' = 0)$ ; Panel C:  $\text{O}_\text{A}+\text{CO}_\text{B}(\nu = 1) \rightarrow \text{O}_\text{B}+\text{CO}_\text{A}(\nu' = 1)$  and Panel D:  $\text{O}_\text{A}+\text{CO}_\text{B}(\nu = 1) \rightarrow \text{O}_\text{B}+\text{CO}_\text{A}(\nu' = 0)$ . For the reactive trajectories (panels C and D), two coordinate systems are used: one for the reactant (black density) in which the  $\text{CO}_\text{B}$  diatom is the distance  $r$  and the separation of atom  $\text{O}_\text{A}$  from the center of mass is the distance  $R$ ; the second coordinate system is for the product state (red density) for which the  $\text{CO}_\text{A}$  diatom is the distance  $r'$  and the separation of atom  $\text{O}_\text{B}$  from the center of mass is the distance  $R'$ . The dashed blue isocontours in panel D are for  $\text{O}_\text{A}+\text{CO}_\text{B}(\nu = 1) \rightarrow \text{O}_\text{B}+\text{CO}_\text{A}(\nu' = 2)$ . The density map for the trajectories is superimposed on a relaxed 2D RKHS PES where  $2.00 < r < 2.30 \text{ a}_0$  (turning points). For all density maps 1500 trajectories were used to generate the 2d densities which were smoothed using kernel density estimation (KDE) as implemented in the R software package.<sup>68</sup>

Panel 8A shows that nonrelaxing trajectories sample regions in the long range without penetrating into the strongly interacting region around  $(R = 3.2\text{a}_0, \theta = 150^\circ)$ . Contrary to that, nonreactive, relaxing trajectories of the type  $\text{O}+\text{CO}(\nu = 1) \rightarrow \text{O}+\text{CO}(\nu' = 0)$  access the strongly interacting region and sample it before leaving this region again, see Figure 8B.

For the reactive trajectories ( $\text{O}_\text{A} + \text{CO}_\text{B} \rightarrow \text{O}_\text{B} + \text{CO}_\text{A}$ ), see Figures 8C and D, all trajectories enter the strongly interacting region along  $\theta \sim 160^\circ$  (black density).

After the reaction, the product ( $\text{CO}_\text{A}$ ) can either remain vibrationally excited (Figure 8C; no relaxation), or its vibrational state can change ( $\text{CO}_\text{A}(v' = 0)$  or  $\text{CO}_\text{A}(v' = 2)$ ). The highest vibrational state in the products after reaction in these trajectories (run at 1000 K) is  $v' = 3$ . The probability distributions of the products from reactive collisions in Figures 8C and D are in red (for  $v' = 0$ , relaxation) and in blue (for  $v' = 2$ , further excitation). The shape of the red and blue probability distributions in Figures 8C and D can already be anticipated from the relaxed PES for the CO+O channel, see Figure S9. Starting from around the minimum on the PES at ( $R = 3.2a_0, \theta = 140^\circ$ ) these densities follow the path indicated by the green isocontour at  $-10.5$  eV in Figure S9 through the constriction indicated as a red cross. A different perspective that could be taken is to refer to all reactive trajectories as “vibrationally relaxing” because the quanta initially present in  $\text{CO}_\text{B}$  are destroyed upon dissociation of  $\text{CO}_\text{B}$ . However, experimentally, the final states  $\text{CO}_\text{B}(v' = 1)$  and  $\text{CO}_\text{A}(v' = 1)$  can not be distinguished. Hence separation into 4 separate cases is meaningful in analyzing the trajectories.

It is also of interest to consider the distribution of contact times  $\tau_c$  for each of the scenarios. This quantity was taken as the first instance along the trajectory for which the sum  $\sigma$  of all three atom distances is smaller than  $12 a_0$  in the entrance channel until the point at which  $\sigma > 12 a_0$  along the exit channel. This was done for CO initially in its  $v = 1$  and  $v = 2$  states, respectively. The average contact times are reported in Table 4 and their distributions are shown in Figure 9. It should, however, be noted that the average  $\tau_c$  only incompletely characterize the underlying distribution  $P(\tau_c)$  because the distributions are either structured (Figures 9a and c) or extend to times more than 10 times the most probable value as in Figures 9b and d.

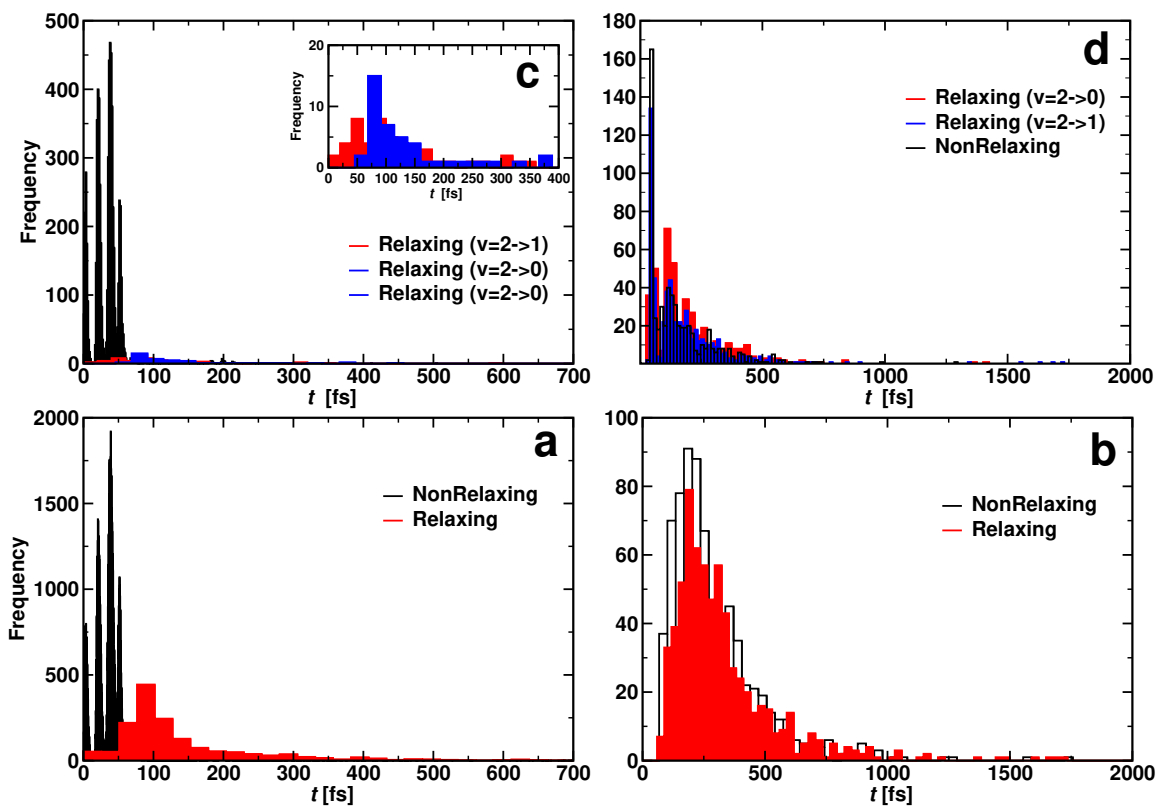


Figure 9: Contact time histogram for  $O_A + CO_B \rightarrow O_B + CO_A$  (reacting: panel a and c) and  $O_A + CO_B \rightarrow O_A + CO_B$  (non reacting: panel b and d). Bottom panels for  $CO(v = 1)$  and top panel for  $CO(v = 2)$ . Panel c inset illustrates that relaxing two quanta ( $\nu = 2 \rightarrow 0$ , blue distribution) takes longer than relaxing one quantum ( $\nu = 2 \rightarrow 1$ , red distribution). Additional analysis of the data from panel c is provided in Figure S10. Rates for the atom exchange reaction are given in Table S5.



For reacting trajectories and non-reacting but relaxing trajectories, the contact time  $\tau_c$  decreases with increasing vibrational excitation. This differs for non-reacting, relaxing trajectories. Their average contact times appear to be determined by the final vibrational state. For relaxation to  $v' = 0$  the average vibrational relaxation time is  $\sim 150$  fs which shortens to  $\sim 70$  fs for relaxation to  $v' = 1$  with initial  $v = 2$ . This is in contrast to the non-relaxing non-reacting trajectories which appear to be independent of vibrational excitation. The  $\tau_c$  for these trajectories is of the order of 30 fs which is roughly the minimum time required for one collision.

When considering the lifetime distributions it is found that those involving reacting trajectories display a regular pattern of peaks, see Figures 9a and c. The specific case for relaxation from  $(v = 1) \rightarrow (v' = 0)$  is shown in Figure S10. It is noticeable that the probability to find trajectories that react but do not relax  $P(\tau_c)$  can be zero and reaches maximal values for other values for the lifetime. Fourier transformation of this signal yields frequencies between  $1824 \text{ cm}^{-1}$  and  $2529 \text{ cm}^{-1}$ , see Figure S10. These frequencies, which are in the range of typical CO stretch frequencies, can be understood as “gating modes” that allow the reaction to occur, similar to what was found for proton transfer in protonated ammonia dimer.<sup>69</sup>

It is also of interest to consider the geometries sampled for the  $\text{C} + \text{O}_2 \rightarrow \text{CO} + \text{O}(^1\text{D})$  reaction on the  $^1\text{A}'$  PES depending on the temperature from which the initial conditions were generated. This was done for  $T = 15 \text{ K}$  and  $T = 10000 \text{ K}$ . For reactive trajectories at low temperature the global minimum is extensively sampled (see Figure S11A) whereas at high temperature this region is not sampled at all as shown in Figure S11B. Hence, collisions at different temperatures are expected to sample complementary regions of the 3d PES.

## Discussion and Conclusions

The present work reports thermal and vibrational relaxation rates from QCT simulations on the five lowest PESs of the [COO] systems. Comparison with experiment is favourable for thermal rates and vibrational relaxation rates at high temperatures. For the atom exchange rate, agreement is rather more qualitative, with an overall offset in the energetics of 300 K (0.026 eV). Additional analyses are carried out in the following to provide an understanding of remaining disagreements between experiment and simulations.

One interesting comparison can be made with state-to-state cross section measurements for the  $\text{C}(^3\text{P}) + \text{O}_2(^3\Sigma_g^-) \leftrightarrow \text{CO}(^1\Sigma^+) + \text{O}(^1\text{D})$  reaction at small collision energies.<sup>34</sup> These experiments used a pulsed nozzle through which the  $\text{O}_2$  expanded into the vacuum. The  $\text{O}_2$  internal state distribution was not measured directly but expected to be very cold.<sup>34</sup> Hence, it is likely that mostly  $\text{O}_2(v = 0)$  with low  $j_{\text{max}}$  was populated. Such experiments found that excitation of  $\text{CO}(v' = 16)$  occurs for all collision energies  $E_c$  whereas population of  $\text{CO}(v' = 17)$  is only possible with an excess of  $E_c > 0.04$  eV. Using bound state energies for CO derived from experiment<sup>70</sup> and accounting for the 0.04 eV required to open the  $\text{CO}(v' = 17)$  channel, the energy difference between  $\text{CO}(v = 0)$  and  $\text{CO}(v' = 17)$  is 4.037 eV. Including zero point energy for CO and  $\text{O}_2$ , the difference between the  $\text{C}(^3\text{P}) + \text{O}_2$  and  $\text{CO} + \text{O}(^3\text{P})$  channels from experimental data is 4.075 eV. This differs by 0.085 eV from the value at the MRCI level of theory which is 3.990 eV.

From semiclassical calculations on the present PESs the  $\text{CO}(v' = 17)$  state is at 4.140 eV. This compares with the difference in electronic energies (3.990 eV) and differences in the CO and  $\text{O}_2$  zero point energies of 3.952 eV. Hence,  $E_c = (4.140 - 3.952) = 0.188$  eV is required to open the  $\text{CO}(v' = 17)$  channel. QCT simulations starting from Boltzmann-distributed  $(v, j)$  initial conditions find that the population of the  $\text{CO}(v' = 16)$  decays exponentially with increasing  $E_c$  (Figure S12 left panel) which is consistent with experiments.<sup>34</sup> Because

expansion through a nozzle does not necessarily yield Boltzmann-distributed initial conditions and the experimental beam was deemed “very cold”,<sup>34</sup> the final state distributions were also separated into those originating from  $O_2(v = 0)$  (open circles in Figure S12) and those from  $O_2(v > 0)$  (solid line in Figure S12). For  $CO(v' = 16)$  all distributions follow the same overall behaviour.

Conversely, for  $CO(v' = 17)$  considering the final state distribution from initial  $O_2(v = 0)$  has an onset at  $\sim 0.05$  eV (inset Figure S12 right panel) with a dependence on  $E_c$  consistent with experiment<sup>34</sup> whereas including all initial  $v$ -states for  $O_2$  and those starting from  $O_2(v > 0)$  again show a decaying probability distribution with increasing  $E_c$ . Because both, initial  $v$  and  $j$  are probably “cold”, it is meaningful to consider final  $CO(v' = 17)$  distributions originating from different  $j_{\max}$  values for the parent  $O_2$  molecule. With decreasing  $j_{\max}$  the  $CO(v' = 17)$  channel opens with increasing values of  $E_c$ . For  $j_{\max}^{O_2} < 30$ , the onset occurs at 0.05 eV and shifts to  $\sim 0.15$  eV for  $j_{\max}^{O_2} < 10$ , which is consistent with the estimate of 0.188 eV based entirely on energetic arguments above. A temperature of  $T = 300$  K corresponds to  $O_2(j = 12)$  but the corresponding (nonequilibrium) distribution probably extends to higher  $j$ -values. Hence an estimated onset of generating  $CO(v' = 17)$  for  $E_c \in [0.05, 0.10]$  eV is expected from the present simulations. This corresponds to a difference of 0.01 eV to 0.06 eV from experiment on a scale of 4 eV, which is an error of 1 % at most.

For the deactivation of  $O(^1D)$  to  $O(^3P)$  in the atmosphere early models performed well for the observed data available at that time.<sup>23</sup> The CO case was categorized as one that is dominated by the configuration of a critical region where a crossing between the single PESs originating from the  $O(^1D)$  channel cross the triplet PESs leading to  $O(^3P)$ . For the crossing dynamics a Landau-Zener model was assumed. This simple approach lead to a predicted rate of  $8.0 \times 10^{-11}$  cm<sup>3</sup> molecule<sup>-1</sup> s<sup>-1</sup> at 300K which was within the error of experimental measurements of 7.6 and  $7.3 \times 10^{-11}$  cm<sup>3</sup> molecule<sup>-1</sup> s<sup>-1</sup>.<sup>14,71</sup> Following this, the deac-

tivation of  $O(^1D)$  by CO was measured and the rate obtained was fit by the expression  $(4.7 \pm 0.9) \times 10^{-11} \exp((126 \pm 33)/RT)$  which yields a rate of  $5.8 \times 10^{-11} \text{ cm}^3 \text{ molecule}^{-1} \text{ s}^{-1}$  at 300 K. Assuming  $\sim 5 \times 10^{-10} \text{ cm}^3 \text{ molecule}^{-1} \text{ s}^{-1}$  for the collision rate, this implies a  $\approx 10\%$  efficiency for deactivation of  $O(^1D)$  to  $O(^3P)$  at 300 K. Based on this low efficiency the crossings between the singlet and triplet manifolds are not expected to have a large impact on the formation, exchange or relaxation of the reaction.

As Tully pointed out, deactivation depends on the specific crossing geometry of the PESs; in this case the singlet and triplet surfaces. Figures S13 and S14 show the crossings of the  $^3A$  with the  $^1A$  surfaces on PESs evaluated at the inner (Figure S13) and outer (Figure S13) turning points for the  $CO(v=0)$  vibration. When starting from the  $CO_A+O_B$  side of the reaction, as was previously mentioned, Figure 8 shows that the active reactions sample a channel near  $140^\circ$  that brings the outgoing  $O_A$  atom into approximately  $R = 3.5 a_0$ . At low temperature, starting from  $CO+O(^3P)$ , it would be possible to cross from any of the  $^3A$  surfaces onto the  $^1A'$  surface to lead to ground state  $CO_2$ . However, in a collisionless environment the complex will still have sufficient energy to return to the  $^1A'$  PES and will have to cross with a  $^3A$  surface to leave as  $O(^3P)$ . This may affect vibrational energy transfer or the exchange reaction and may be the reason for the shifts in the onset seen between the experiment and QCT such as in Figure 7 at low temperature. Starting from  $CO+O(^1D)$  and traveling along the  $^1A'$  surface crosses all  $^3A$  surfaces while the  $(2)^1A'$  and  $^1A''$  surfaces only cross the repulsive  $(2)^3A''$  surface. At temperatures lower than that required to form  $C(^3P)+O_2$  these trajectories can potentially cross on to the  $^3A$  surfaces and then return to the  $CO+O(^3P)$  state although it would be at high CO vibrational state.

One finding of the present work is the role “gating” plays in the different processes considered here. For one, vibrational relaxation with atom exchange displays gating in the contact time distributions which hints at a time-dependent barrier in the  $[COO]$  collision

complex. This is explicitly seen in the barriers for the  $\text{CO}_A(^1\Sigma^+) + \text{O}_B(^3\text{P}) \rightarrow \text{CO}_B(^1\Sigma^+) + \text{O}_A(^3\text{P})$  atom exchange reaction on the  $^3\text{A}'$  PES (Figure S8). Depending on the phase of the CO vibration at which the impinging oxygen atom collides with the diatomic molecule, the barrier for formation of the collision complex is either high or low. Such processes are particularly susceptible to zero-point vibrational effects which can not be captured in QCT simulations. Specifically, the vibrational wavefunction does not produce the same spatial probability distribution at low  $v$  as the classical trajectory. This results in differences in sampling times for when the gate is open versus closed. The rates from QCT simulations should, therefore, underestimate the true rates, in particular at low temperatures. This is indeed found for vibrational relaxation, see Figure 7 and for the atom exchange reaction S6. As the vibrational relaxation rates include both, processes with and without atom exchange, and the CO vibration-dependent barriers only affect trajectories with atom exchange, it is conceivable that vibrational relaxation without atom exchange is not affected by these effects.

Including zero-point effects is likely to improve the comparison between calculations and experiments. Furthermore, nonadiabatic effects may further improve comparison with experiment, in particular for the processes leading from  $\text{CO}_2$  to the  $\text{O}+\text{CO}$  asymptotes. Analysis of vibrational relaxation demonstrates that depending on the process considered (with or without reaction), different parts of the fully-dimensional PES are sampled. This is also true for reactions at low (15 K) and higher (1000 K) temperatures, respectively. Together with suitable information from experiment the underlying PESs could be further improved from techniques such as morphing<sup>72,73</sup> or Bayesian inference.<sup>74</sup>

In conclusion, the present work provides a comprehensive characterization of the energetics and dynamics of the reactive  $[\text{COO}]$  system involving the lowest five electronic states. Many findings provide good agreement between simulations and experiments but it is also found that disagreements can be traced back to neglecting quantum mechanical effects at low tem-

peratures. Additional experiments for this important system will provide a more complete understanding of the reactions involving both asymptotes.

## Acknowledgments

This work was supported by the Swiss National Science Foundation through grants 200021-117810, and the NCCR MUST.

## References

- (1) Sharma, M.; Swantek, A. B.; Flaherty, W.; Austin, J. M.; Doraiswamy, S.; Candler, G. V. Experimental and Numerical Investigation of Hypervelocity Carbon Dioxide Flow over Blunt Bodies. *J. Thermophys. Heat Transf.* **2010**, *24*, 673–683.
- (2) Lewittes, M. E.; Davis, C. C.; McFarlane, R. A. Vibrational deactivation of CO( $v = 1$ ) by oxygen atoms. *J. Chem. Phys.* **1978**, *69*, 1952–1957.
- (3) Husain, D.; Young, A. N. Kinetic investigation of ground state carbon atoms, C( $2^3P$ ). *J. Chem. Soc., Faraday Trans. 2* **1975**, *71*, 525–531.
- (4) Bergeat, A.; Calvo, T.; Dorthe, G.; Loison, J. Fast-flow study of the C plus NO and C+O<sub>2</sub> reactions. *Chem. Phys. Lett.* **1999**, *308*, 7–12.
- (5) Geppert, W. D.; Reignier, D.; Stoecklin, T.; Naulin, C.; Costes, M.; Chastaing, D.; Le Picard, S. D.; Sims, I. R.; Smith, I. W. M. Comparison of the cross-sections and thermal rate constants for the reactions of C( $3P$ ) atoms with O<sub>2</sub> and NO. *Phys. Chem. Chem. Phys.* **2000**, *2*, 2873–2881.
- (6) Becker, K. H.; Brockmann, K. J.; Weisen, P. Spectroscopic identification of C( $3P$ ) atoms in halogenomethane + H flame systems and measurements of C( $3P$ ) reaction rate

- constants by two-photon laser-induced fluorescence. *J. Chem. Soc., Faraday Trans. 2* **1988**, *84*, 455–461.
- (7) Dorthe, G.; Caubet, P.; Vias, T.; Barrere, B.; Marchais, J. Fast flow studies of atomic carbon kinetics at room temperature. *J. Phys. Chem.* **1991**, *95*, 5109–5116.
- (8) Chastaing, D.; L. James, P.; R. Sims, I.; W. M. Smith, I. Neutral–neutral reactions at the temperatures of interstellar clouds: Rate coefficients for reactions of atomic carbon, C(<sup>3</sup>P), with O<sub>2</sub>, C<sub>2</sub>H<sub>2</sub>, C<sub>2</sub>H<sub>4</sub> and C<sub>3</sub>H<sub>6</sub> down to 15 K. *Phys. Chem. Chem. Phys.* **1999**, *1*, 2247–2256.
- (9) Chastaing, D.; Le Picard, S. D.; Sims, I. R. Direct kinetic measurements on reactions of atomic carbon, C(<sup>3</sup>P), with O<sub>2</sub> and NO at temperatures down to 15 K. *J. Chem. Phys.* **2000**, *112*, 8466–8469.
- (10) Dean, A. J.; Davidson, D. F.; Hanson, R. K. A shock tube study of reactions of carbon atoms with hydrogen and oxygen using excimer photolysis of C<sub>3</sub>O<sub>2</sub> and carbon atom atomic resonance absorption spectroscopy. *J. Phys. Chem.* **1991**, *95*, 183–191.
- (11) Ogryzlo, E.; Reilly, J.; Thrush, B. Vibrational excitation of CO from the reaction C+O<sub>2</sub>. *Chem. Phys. Lett.* **1973**, *23*, 37–39.
- (12) Dubrin, J.; MacKay, C.; Pandow, M.; Wolfgang, R. Reactions of atomic carbon with  $\pi$ -bonded inorganic molecules. *J. Inorg. Nuc. Chem.* **1964**, *26*, 2113–2122.
- (13) Xantheas, S. S.; Ruedenberg, K. Potential energy surfaces of carbon dioxide. *Int. J. Quantum Chem.* **1994**, *49*, 409–427.
- (14) Heidner, R. F.; Husain, D.; Wiesenfeld, J. R. Kinetic investigation of electronically excited oxygen atoms, O(2<sup>1</sup>D<sub>2</sub>), by time-resolved attenuation of atomic resonance radiation in the vacuum ultra-violet. Part 2. Collisional quenching by the atmospheric gases N<sub>2</sub>, O<sub>2</sub>, CO, CO<sub>2</sub>, H<sub>2</sub>O and O<sub>3</sub>. *Faraday Discuss.* **1973**, *69*, 927–938.

- (15) Heidner, R.; Husain, D. Quenching of O( $2^1D_2$ ) by atmospheric gases. *Nat. Phys. Sci.* **1973**, *241*, 10–11.
- (16) Jasper, A. W.; Dawes, R. Non-Born–Oppenheimer molecular dynamics of the spin-forbidden reaction O( $^3P$ ) + CO( $X^1\Sigma^+$ )  $\rightarrow$  CO $_2$ ( $X^1\Sigma_g^+$ ). *J. Chem. Phys.* **2013**, *139*, 154313.
- (17) Troe, J. *Fifth Symp. (Int.) Combust.* **1975**, *15*, 667–679.
- (18) Braunstein, M.; Duff, J. W. Electronic structure and dynamics of O( $^3P$ ) + CO( $^1\Sigma^+$ ) collisions. *J. Chem. Phys.* **2000**, *112*, 2736–2745.
- (19) Kozlov, P.; Makarov, V.; Pavlov, V.; Shatalov, O. Experimental investigation of CO vibrational deactivation in a supersonic cooling gas flow. *Shock Waves* **2000**, *10*, 191–195.
- (20) Center, R. E. Vibrational relaxation of CO by O atoms. *J. Chem. Phys.* **1973**, *58*, 5230–5236.
- (21) Kelley, J. D.; Thommarson, R. L. Vibrational deactivation and atom exchange in O( $^3P$ ) + CO( $X^1\Sigma^+$ ) collisions. *J. Chem. Phys.* **1977**, *66*, 1953–1959.
- (22) Davidson, J. A.; Schiff, H. I.; Brown, T. J.; Howard, C. J. Temperature dependence of the deactivation of O( $^1D$ ) by CO from 113 to 333 K. *J. Chem. Phys.* **1978**, *69*, 1216–1217.
- (23) Tully, J. C. Reactions of O( $^1D$ ) with atmospheric molecules. *J. Chem. Phys.* **1975**, *62*, 1893–1898.
- (24) Winter, N. W.; Bender, C. F.; Goddard III, W. A. Theoretical assignments of the low-lying electronic states of carbon dioxide. *Chemical Physics Letters* **1973**, *20*, 489–492.



- (25) Grebenshchikov, S. Y.; Borrelli, R. Crossing Electronic States in the Franck-Condon Zone of Carbon Dioxide: A Five-Fold Closed Seam of Conical and Glancing Intersections. *J. Phys. Chem. Lett.* **2012**, *3*, 3223–3227.
- (26) Grebenshchikov, S. Y. Photodissociation of carbon dioxide in singlet valence electronic states. II. Five state absorption spectrum and vibronic assignment. *J. Chem. Phys.* **2013**, *138*, 224107.
- (27) Grebenshchikov, S. Y. Photodissociation of carbon dioxide in singlet valence electronic states. I. Six multiply intersecting ab initio potential energy surfaces. *J. Chem. Phys.* **2013**, *138*, 224106.
- (28) Schmidt, J. A.; Johnson, M. S.; Schinke, R. Carbon dioxide photolysis from 150 to 210 nm: Singlet and triplet channel dynamics, UV-spectrum, and isotope effects. *Proc. Natl. Acad. Sci.* **2013**, *110*, 17691–17696.
- (29) Zhou, B.; Zhu, C.; Wen, Z.; Jiang, Z.; Yu, J.; Lee, Y.-P.; Lin, S. H. Topology of conical/surface intersections among five low-lying electronic states of CO<sub>2</sub>: Multireference configuration interaction calculations. *J. Chem. Phys.* **2013**, *139*.
- (30) Dixon, R. N.; Porter, G. The carbon monoxide flame bands. *Proc. R. Soc. Lond. A.* **1963**, *275*, 431–446.
- (31) Kinnersly, S.; Murrell, J. A classical dynamical study of the reaction between C(<sup>3</sup>P) and O<sub>2</sub>(<sup>3</sup>Σ<sub>g</sub><sup>-</sup>). *Mol. Phys.* **1977**, *33*, 1479–1494.
- (32) Brunsvold, A. L.; Upadhyaya, H. P.; Zhang, J.; Cooper, R.; Minton, T. K.; Braunstein, M.; Duff, J. W. Dynamics of Hyperthermal Collisions of O(<sup>3</sup>P) with CO. *J. Phys. Chem. A* **2008**, *112*, 2192–2205.
- (33) Schwenke, D. W.; Jaffe, R. L.; Chaban, G. M. Collisional dissociation of CO: ab initio

- potential energy surfaces and quasiclassical trajectory rate coefficients. "unpublished" **2016**, 1–56.
- (34) Costes, M.; Naulin, C. State-to-state cross sections for the  $C(^3P_J) + O_2(X^3\Sigma_g^-) \rightarrow CO(X^1\Sigma^+) + O(^1D_2)$  reaction at kinetic energies between 4.4 and 90 meV. *Comptes Rendus de l'Académie des Sciences-Series IIC-Chemistry* **1998**, *1*, 771–775.
- (35) Dean, A. J.; Davidson, D. F.; Hanson, R. K. A shock tube study of reactions of carbon atoms with hydrogen and oxygen using excimer photolysis of  $C_3O_2$  and carbon atom atomic resonance absorption spectroscopy. *J. Phys. Chem.* **1991**, *95*, 183–191.
- (36) Ho, T.-S.; Rabitz, H. A general method for constructing multidimensional molecular potential energy surfaces from ab initio calculations. *J. Chem. Phys.* **1996**, *104*, 2584.
- (37) Unke, O. T.; Meuwly, M. Toolkit for the Construction of Reproducing Kernel-Based Representations of Data: Application to Multidimensional Potential Energy Surfaces. *J. Chem. Inf. Model* **2017**, *57*, 1923–1931.
- (38) Werner, H.-J.; Knowles, P. J. An efficient internally contracted multiconfiguration-reference configuration interaction method. *J. Chem. Phys.* **1988**, *89*, 5803–5814.
- (39) Knowles, P. J.; Werner, H.-J. An efficient method for the evaluation of coupling coefficients in configuration interaction calculations. *Chem. Phys. Lett.* **1988**, *145*, 514 – 522.
- (40) Langhoff, S.; Davidson, E. Configuration interaction calculations on nitrogen molecule. *Int. J. Quant. Chem.* **1974**, *8*, 61–72.
- (41) Dunning, T. H. Gaussian basis sets for use in correlated molecular calculations. I. The atoms boron through neon and hydrogen. *J. Chem. Phys.* **1989**, *90*, 1007–1023.
- (42) Werner, H.-J.; Knowles, P. J.; Knizia, G.; Manby, F. R.; et al., M. S. MOLPRO, version 2019.1, A package of ab initio programs. 2019.

- (43) Werner, H.-J.; Knowles, P. J. A second order multiconfiguration SCF procedure with optimum convergence. *J. Chem. Phys.* **1985**, *82*, 5053–5063.
- (44) Knowles, P. J.; Werner, H.-J. An efficient second-order MC SCF method for long configuration expansions. *Chem. Phys. Lett.* **1985**, *115*, 259 – 267.
- (45) Werner, H.-J.; Meyer, W. A quadratically convergent multiconfiguration–self-consistent field method with simultaneous optimization of orbitals and CI coefficients. *J. Chem. Phys.* **1980**, *73*, 2342–2356.
- (46) Kreplin, D. A.; Knowles, P. J.; Werner, H.-J. Second-order MCSCF optimization revisited. I. Improved algorithms for fast and robust second-order CASSCF convergence. *J. Chem. Phys.* **2019**, *150*, 194106.
- (47) Ho, T.-S.; Rabitz, H. Proper construction of ab initio global potential surfaces with accurate long-range interactions. *J. Chem. Phys.* **2000**, *113*, 3960–3968.
- (48) Henkelman, G.; Uberuaga, B.; Jonsson, H. A climbing image nudged elastic band method for finding saddle points and minimum energy paths. *J. Chem. Phys.* **2000**, *113*, 9901–9904.
- (49) Larsen, A. H.; Mortensen, J. J. The atomic simulation environment—a Python library for working with atoms. *J. Phys. Condens. Matter* **2017**, *29*, 273002.
- (50) Truhlar, D. G.; Muckerman, J. T. In *Atom - Molecule Collision Theory*; Bernstein, R. B., Ed.; Springer US, 1979; pp 505–566.
- (51) Henriksen, N. E.; Hansen, F. Y. *Theories of Molecular Reaction Dynamics*; Oxford, 2011.
- (52) Koner, D.; Barrios, L.; González-Lezana, T.; Panda, A. N. State-to-State Dynamics of the  $\text{Ne} + \text{HeH}^+(v = 0, j = 0) \rightarrow \text{NeH}^+(v', j') + \text{He}$  Reaction. *J. Phys. Chem. A* **2016**, *120*, 4731–4741.

- (53) Koner, D.; Bemish, R. J.; Meuwly, M. The  $C(^3P) + NO(X^2\Pi) \rightarrow O(^3P) + CN(X^2\Sigma^+)$ ,  $N(^2D)/N(^4S) + CO(X^1\Sigma^+)$  reaction: Rates, branching ratios, and final states from 15 K to 20 000 K. *J. Chem. Phys.* **2018**, *149*, 094305.
- (54) Bonnet, L.; Rayez, J.-C. Quasiclassical Trajectory Method for Molecular Scattering Processes: Necessity of a Weighted Binning Approach. *Chem. Phys. Lett.* **1997**, *277*, 183–190.
- (55) Bonnet, L.; Rayez, J.-C. Gaussian Weighting in the Quasiclassical Trajectory Method. *Chem. Phys. Lett.* **2004**, *397*, 106–109.
- (56) Shen, V. K.; Siderius, D. W.; Krekelberg, W. P.; ; Hatch, H. W.; Eds., *NIST Chemistry WebBook, NIST Standard Reference Database Number 69*.
- (57) Hwang, D.-Y.; Mebel, A. M. Ab initio study of spin-forbidden unimolecular decomposition of carbon dioxide. *cp* **2000**, *256*, 169 – 176.
- (58) Braunstein, M.; Duff, J. W. Classical Collision Spectrum of  $O + CO$ . *J. Phys. Chem. A* **2009**, *113*, 10795–10802.
- (59) Fairbairn, A. R.; Gaydon, A. G. The dissociation of carbon monoxide. *Proc. Royal Soc. Lond. A*. **1969**, *312*, 207–227.
- (60) Bergeat, A.; Calvo, T.; Dorthe, G.; Loison, J. Fast-flow study of the  $C+NO$  and  $C+O_2$  reactions. *Chem. Phys. Lett.* **1999**, *308*, 7–12.
- (61) Husain, D.; Young, A. N. Kinetic investigation of ground state carbon atoms,  $C(^2^3P)$ . *J. Chem. Soc., Faraday Trans. 2* **1975**, *71*, 525–531.
- (62) Sims, I. R. Low-Temperature Reactions Tunnelling in space. *Nat. Chem.* **2013**, *5*, 734–736.

- (63) Malcolm W. Chase, J. *NIST-JANAF thermochemical tables*; Fourth edition. Washington, DC: American Chemical Society ; New York : American Institute of Physics for the National Institute of Standards and Technology, 1998.
- (64) Jaffe, S.; Klein, F. S. Isotopic exchange reactions of atomic oxygen produced by the photolysis of NO<sub>2</sub> at 3660 Å. *Trans. Faraday Soc.* **1966**, *62*, 3135–3141.
- (65) Garnett, S. H.; Kistiakowsky, G. B.; O Grady, B. V. Isotopic Exchange between Oxygen and Carbon Monoxide in Shock Waves. *J. Chem. Phys.* **1969**, *51*, 84–91.
- (66) Koner, D. *Scattering studies of proton transfer reactions between rare gas atoms*; Indian Institute of Technology Guwahati, 2016.
- (67) Parzen, E. On Estimation of a Probability Density Function and Mode. *The Annals of Mathematical Statistics* **1962**, *33*, 1065–1076.
- (68) Team, R. C. R: A Language and Environment for Statistical Computing. R Foundation for Statistical Computing: Vienna, Austria, 2017.
- (69) Meuwly, M.; Karplus, M. Simulation of proton transfer along ammonia wires: An “ab initio” and semiempirical density functional comparison of potentials and classical molecular dynamics. *J. Chem. Phys.* **2002**, *116*, 2572–2585.
- (70) Chandra, S.; Maheshwari, V.; Sharma, A. Einstein A-coefficients for vib-rotational transitions in CO. *Astronomy and Astrophysics Supplement Series* **1996**, *117*, 557–559.
- (71) Braun, W.; Brown, R. L.; Garvin, D.; Herron, J. T.; Huie, R. E.; Kurylo, M. J.; Laufer, A. H.; McKinley, J. D.; Okabe, H.; Scheer, M. D.; Tsang, W.; Stedman, D. H. Survey of Photochemical and Rate Data for Twenty-eight Reactions of Interest in Atmospheric Chemistry. *Journal of Physical and Chemical Reference Data* **1973**, *2*, 267–312.

- (72) Meuwly, M.; Hutson, J. Morphing ab initio potentials: A systematic study of Ne-HF. *J. Chem. Phys.* **1999**, *110*, 8338–8347.
- (73) Bowman, J. M.; Gazdy, B. A simple method to adjust potential energy surfaces: Application to HCO. *J. Chem. Phys.* **1991**, *94*, 816–817.
- (74) Venturi, S.; Jaffe, R. L.; Panesi, M. A Bayesian Machine Learning Approach to the Quantification of Uncertainties on Ab Initio Potential Energy Surfaces. *J. Phys. Chem. A* **2020**, *124*, 5129–5146.

**Supporting Information: The  $\text{C}(^3\text{P}) + \text{O}_2(^3\Sigma_g^-)$   
 $\leftrightarrow \text{CO}_2 \leftrightarrow \text{CO}(^1\Sigma^+) + \text{O}(^1\text{D})/\text{O}(^3\text{P})$  Reaction:  
Thermal and Vibrational Relaxation Rates from  
15 K to 20000 K**

Juan Carlos San Vicente Veliz,<sup>†</sup> Debasish Koner,<sup>†</sup> Max Schwilk,<sup>†</sup> Raymond J.  
Bemish,<sup>‡</sup> and Markus Meuwly<sup>\*,†,¶</sup>

<sup>†</sup>*Department of Chemistry, University of Basel, Klingelbergstrasse 80, CH-4056 Basel,  
Switzerland*

<sup>‡</sup>*Air Force Research Laboratory, Space Vehicles Directorate, Kirtland AFB, New Mexico  
87117, USA*

<sup>¶</sup>*Department of Chemistry, Brown University, RI, USA*

E-mail: m.meuwly@unibas.ch

March 12, 2021

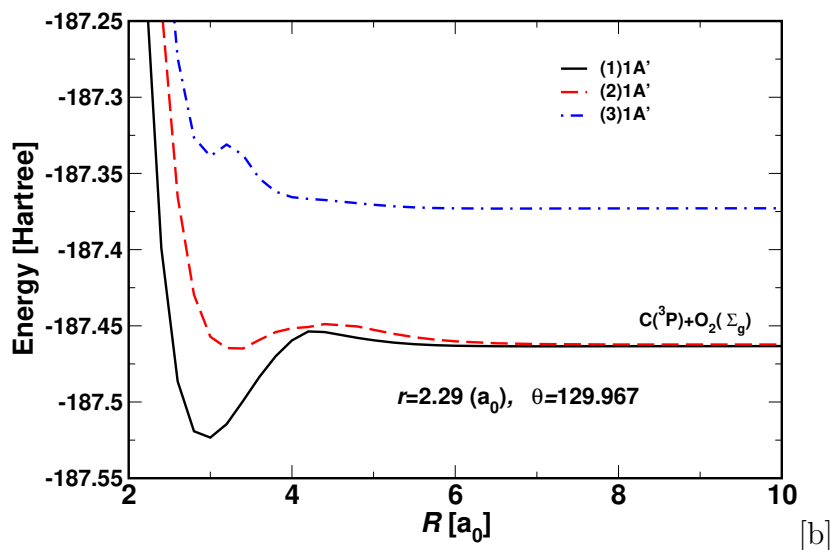


Figure S1: Dissociation curves for  $C(^3P) + O_2(^3\Sigma_g^-)$  at  $r_{O-O} = 2.29 a_0$  and  $\theta = 129.96^\circ$  with varying  $R$ . Calculations at SA-CASSCF level with 3 considered states of the singlet  $^1A'$  state.

## References

- (1) Jaffe, S.; Klein, F. S. Isotopic exchange reactions of atomic oxygen produced by the photolysis of  $NO_2$  at 3660 Å. *Trans. Faraday Soc.* **1966**, *62*, 3135–3141.
- (2) Garnett, S. H.; Kistiakowsky, G. B.; O Grady, B. V. Isotopic Exchange between Oxygen and Carbon Monoxide in Shock Waves. *J. Chem. Phys.* **1969**, *51*, 84–91.
- (3) Costes, M.; Naulin, C. State-to-state cross sections for the  $C(^3P_J) + O_2(X^3\Sigma_g^-) \rightarrow CO(X^1\Sigma^+) + O(^1D_2)$  reaction at kinetic energies between 4.4 and 90 meV. *Comptes Rendus de l'Académie des Sciences-Series IIC-Chemistry* **1998**, *1*, 771–775.



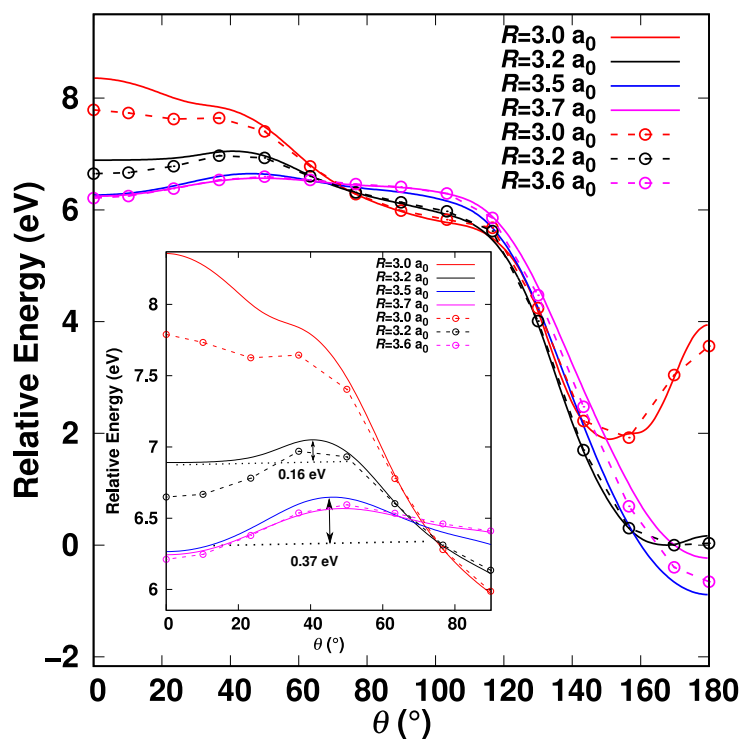


Figure S2: Angular cuts through the  $^1A'$  MRCI-PES (red) and CCSD(T) (black) for different values of  $R$ . At both levels of theory the COO structure is found to be a local minimum, stabilized by  $\sim 9$  (MRCI) and  $\sim 5$  kcal/mol (0.39 and 0.22 eV) (CCSD(T)), respectively. The energy of the COO conformation lies 170 kcal/mol (7.37 eV) above the global minimum. The zero of energy is the minimum for  $R = 3.2 a_0$  for both the MRCI-RKHS (solid lines) and *ab-initio* CCSD(T) (open circles and dashed lines), using the aug-cc-pVTZ basis set in both calculations.

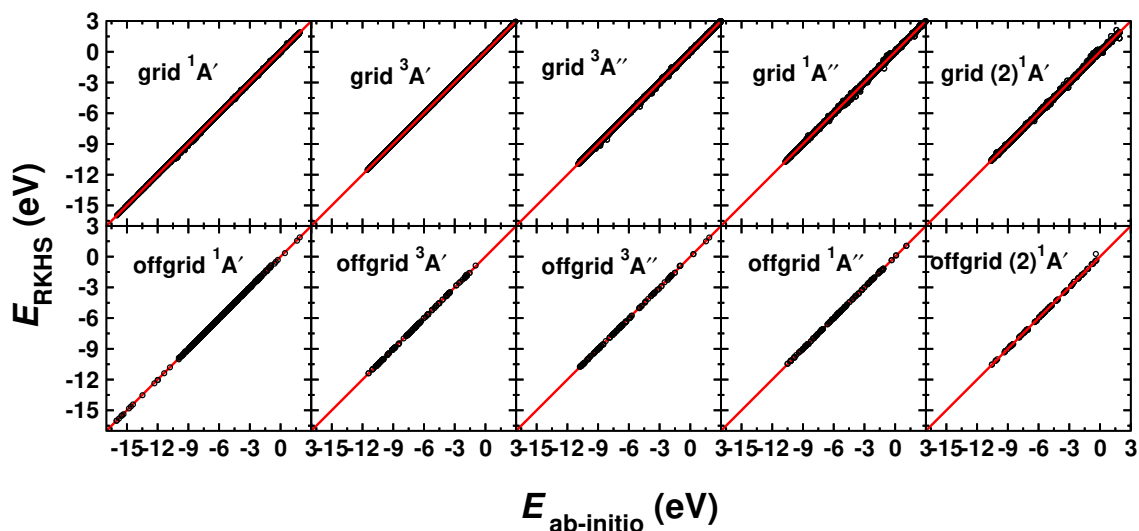


Figure S3: Correlation between MRCI/aug-cc-PVTZ ( $x$ -axis) and RKHS energies ( $y$ -axis) for 23230 ( $^1A'$ ), 9114 ( $^3A'$ ), 20076 ( $^3A''$ ), 19560 ( $^1A''$ ), and 20696 ( $(2)^1A'$ ) for grid points and 618, 201, 194, 188 and 134 offgrid points for the  $^1A'$ ,  $^3A'$ ,  $^3A''$ ,  $^1A''$ , and  $(2)^1A'$  surfaces, respectively. The zero of energy is the O+O+C dissociation limit. The  $R^2$  value for the grid points are (0.99998, 0.99999, 0.99996, 0.99984, 0.99984) and for off-grid points (0.99993, 0.99991, 0.99990, 0.99991, 0.99941) for the ( $^1A'$ ,  $^3A'$ ,  $^3A''$ ,  $^1A''$ ) surfaces, respectively. The corresponding root mean squared errors (RMSE) for the  $^1A'$ ,  $^3A'$ ,  $^3A''$ ,  $^1A''$  and  $(2)^1A'$  surfaces are (0.01, 0.01, 0.02, 0.05, 0.04) eV (0.33, 0.27, 0.56, 1.04, 0.81) kcal/mol for the grid points and (0.03, 0.03, 0.04, 0.03, 0.03) eV (0.65, 0.72, 0.89, 0.59, 0.75) kcal/mol for offgrid points.

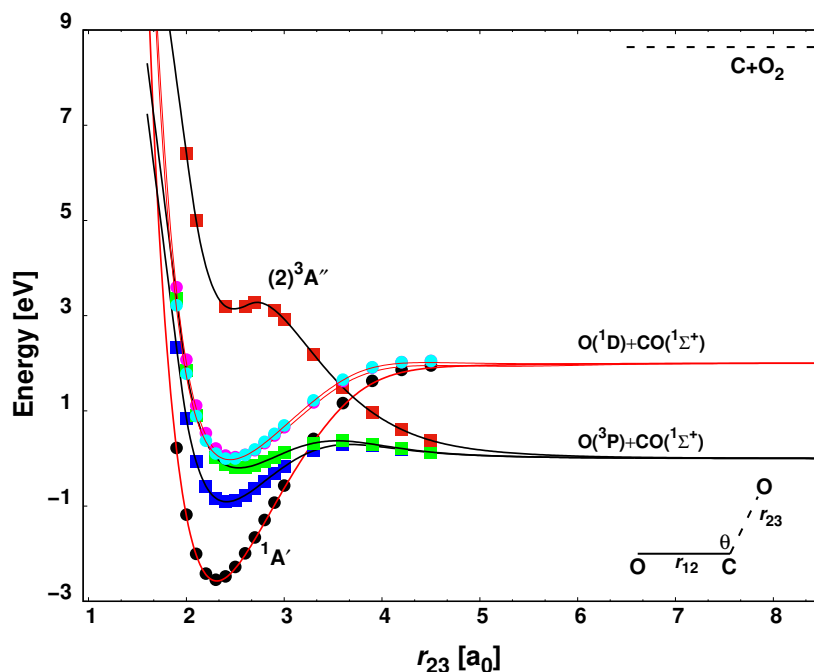


Figure S4: Ab initio calculated (points) and RKHS energies (solid lines) at a fixed CO bond length  $1.2 \text{ \AA}$  ( $2.267 \text{ eV}$ ) and OCO angle  $\theta = 120.0^\circ$  for the  $1A'$  (black solid circle),  $2^1A'$  (cyan solid circle),  $1A''$  (magenta solid circle),  $3A'$  (blue solid square),  $3A''$  (green solid square),  $2^3A''$  (red solid square).

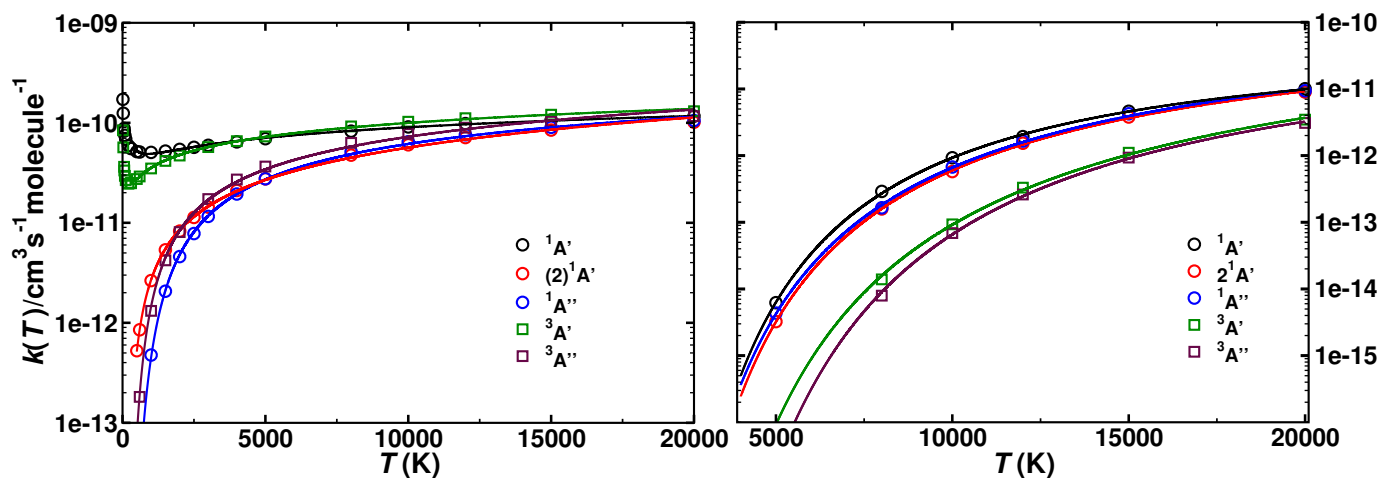


Figure S5: Rates for the forward (left) and reverse (right) reactions involving all five PESs. Symbols are the QCT results and solid lines are the fits to the modified Arrhenius equation. Circles for the rates on the singlet PESs and squares for those on the triplet PESs. Note the different scales along the  $y$ -axis for the forward and reverse rates.

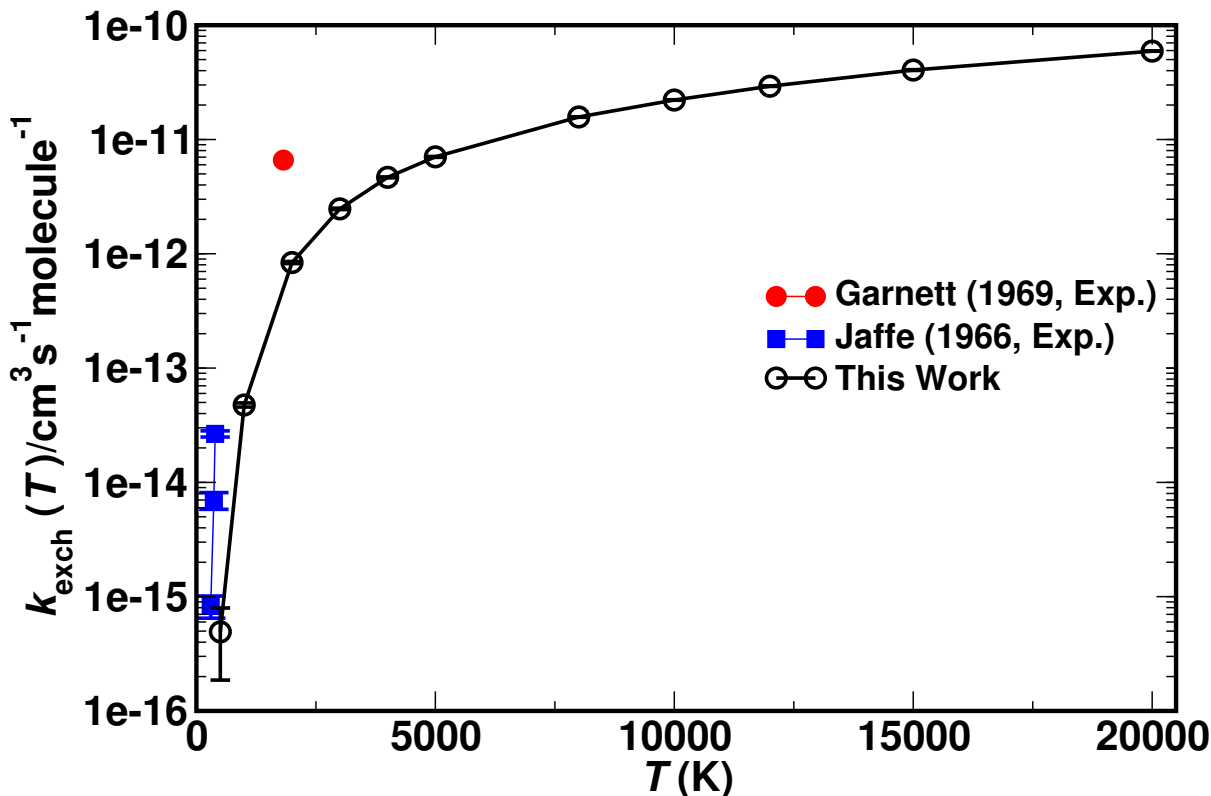


Figure S6: Comparison of computed and experimentally observed<sup>1,2</sup> rates for the  $\text{CO}_A(^1\Sigma^+) + \text{O}_B(^3\text{P}) \rightarrow \text{CO}_B(^1\Sigma^+) + \text{O}_A(^3\text{P})$  exchange reaction. At low temperatures<sup>1</sup> the computations are in better agreement with experiment than for the only high-temperature measurement.<sup>2</sup>

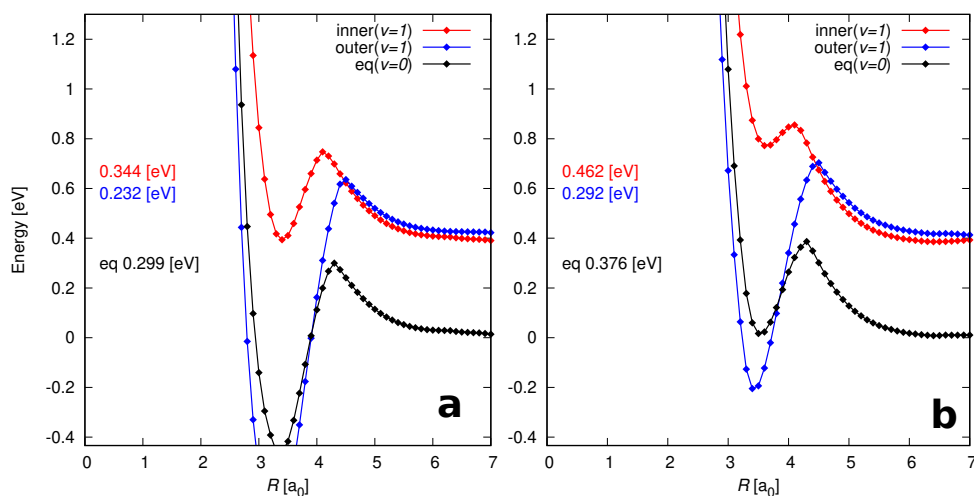


Figure S7: One-dimensional potential energy curves for the  $\text{CO}_A(^1\Sigma^+) + \text{O}_B(^3\text{P}) \rightarrow \text{CO}_B(^1\Sigma^+) + \text{O}_A(^3\text{P})$  atom exchange reaction on the  $^3A'$  (left) and  $^3A''$  PESs. The curves are drawn for fixed CO bond length at the equilibrium (black), ( $v = 1$ ) inner (red), and ( $v = 1$ ) outer (blue) turning points. For both electronic states the barrier height experienced by the approaching oxygen atom  $\text{O}_B$  depends on the separation of the  $\text{CO}_A$  diatom.

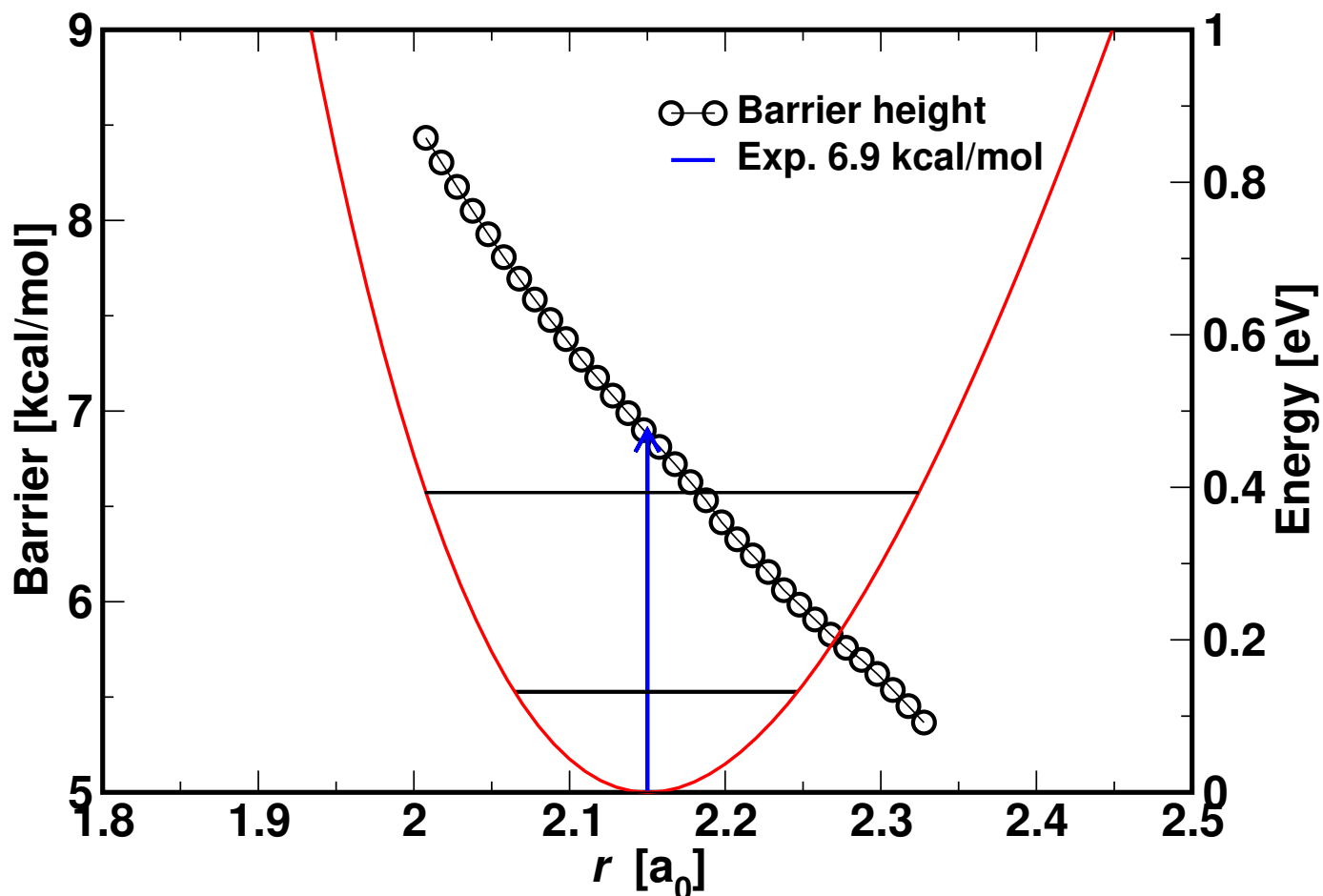


Figure S8: The barrier for the  $\text{CO}_A(^1\Sigma^+) + \text{O}_B(^3\text{P}) \rightarrow \text{CO}_B(^1\Sigma^+) + \text{O}_A(^3\text{P})$  atom exchange reaction on the  $^3\text{A}'$  PES evaluated for CO separations between the inner and outer turning points for  $v_{\text{CO}} = 1$ . The CO potential with the  $v = 0$  and  $v = 1$  state is superimposed. The figure clarifies that the barrier towards formation of  $\text{CO}_2$  varies between 8.5 kcal/mol (0.369 eV) and 5.5 kcal/mol (0.239 eV) at the inner and outer  $v = 1$  turning points. Hence, the CO vibration acts as a gating mode. The barrier height for the isotopic exchange reaction at 300 K was reported<sup>1</sup> to be 6.9 kcal/mol (0.299 eV), consistent with the barriers found here.

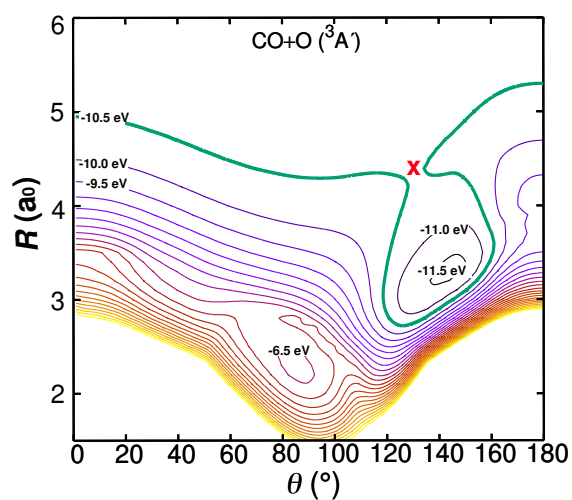


Figure S9: Relaxed 2D-PES for the CO + O asymptote for the  $^3A'$  state. The diatomic distance  $r$  ranges from 2.1  $a_0$  to 3.0  $a_0$ . Contour lines are separated by 0.5 eV between 0 and -11.5 eV with the C+O+O dissociation energy as the zero of energy. The solid green line represents the -10.5 eV isocontour as a reference. It is noted that the relaxing and reactive trajectories leave the strongly interacting region through the opening, indicated by the red cross, around  $R \sim 4.0 a_0$  and  $\theta = 130^\circ$ .

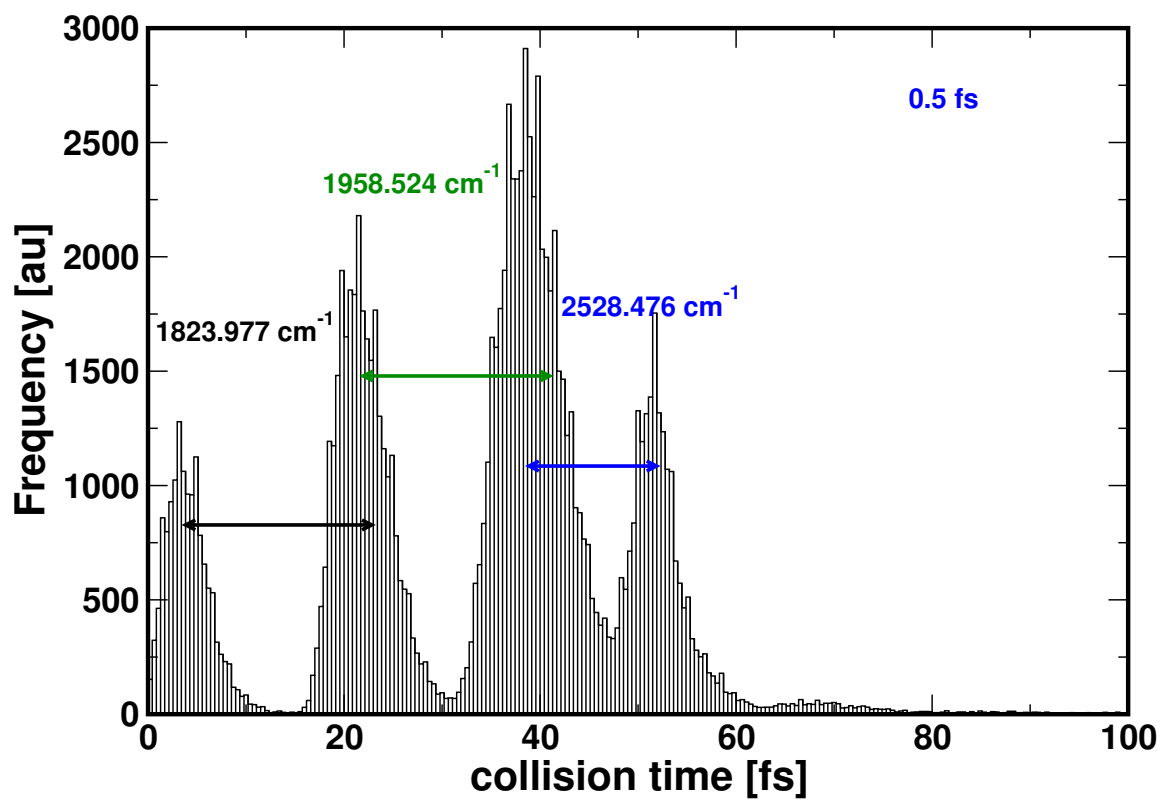


Figure S10: Collision time histogram for  $\nu = 1$ . Difference between adjacent peaks are displayed in  $\text{cm}^{-1}$

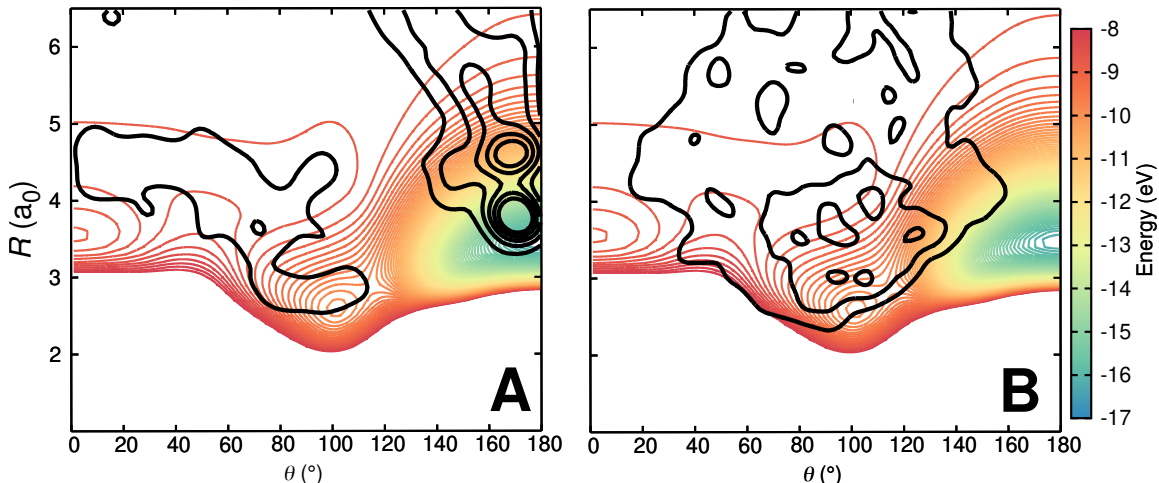


Figure S11: Density trajectory map at 15 K (panel A) and 10000 K (panel B) for the  $\text{C}+\text{O}_2 \rightarrow \text{CO}+\text{O}({}^1\text{D})$  reactive collisions on the ground state  ${}^1\text{A}'$  PES. The density map for the trajectories is superimposed on a relaxed 2D RKHS PES where  $2.00 < r < 2.30 a_0$  (turning points). 300 reacting trajectories were taken for each case and represented as a KDE. It is found that although both sets of trajectories describe the same physical process (atom exchange reaction) they are sensitive to and sample different parts of the PES.

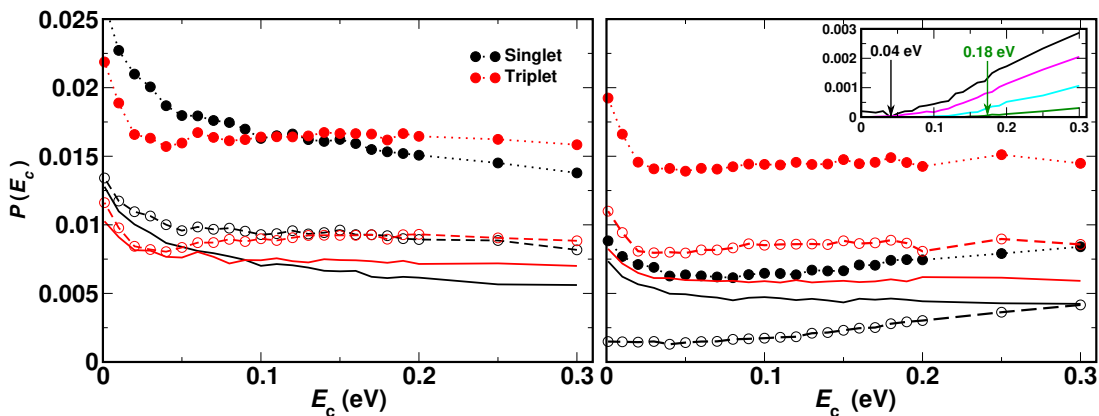


Figure S12: Reaction probability  $P(E_c)$  as a function of collision energy  $E_c$  for the  $\text{C}({}^3\text{P}) + \text{O}_2({}^3\Sigma_g^-) \rightarrow \text{CO}({}^1\Sigma^+) + \text{O}({}^1\text{D})$  (singlet (black),  ${}^1\text{A}'$  PES) and  $\text{C}({}^3\text{P}) + \text{O}_2({}^3\Sigma_g^-) \rightarrow \text{CO}({}^1\Sigma^+) + \text{O}({}^3\text{P})$  (triplet (red),  ${}^3\text{A}'$  PES) reaction. Left panel for final vibrational state  $\text{CO}(v' = 16)$  and right panel for  $\text{CO}(v' = 17)$ . At least  $10^5$  trajectories were run for each collision energy (0.001-0.300 eV). Filled circles: total reaction probability; open circles: reaction probability originating from  $\text{O}_2(v = 0)$ ; solid line: reaction probability originating from  $\text{O}_2(v > 0)$ . The inset in the right hand panel shows an enlargement for the singlet channel (forming  $\text{O}({}^1\text{D})$ ) and highlights the threshold energy observed from experiment<sup>3</sup> to open this product channel at  $E_c = 0.04$  eV. The green, cyan, magenta, and black traces correspond to initial  $\text{O}_2(v = 0, j_{\text{max}} < 10)$ ,  $\text{O}_2(v = 0, j_{\text{max}} < 20)$ ,  $\text{O}_2(v = 0, j_{\text{max}} < 30)$ , and  $\text{O}_2(v = 0)$  for all  $j$ -values.



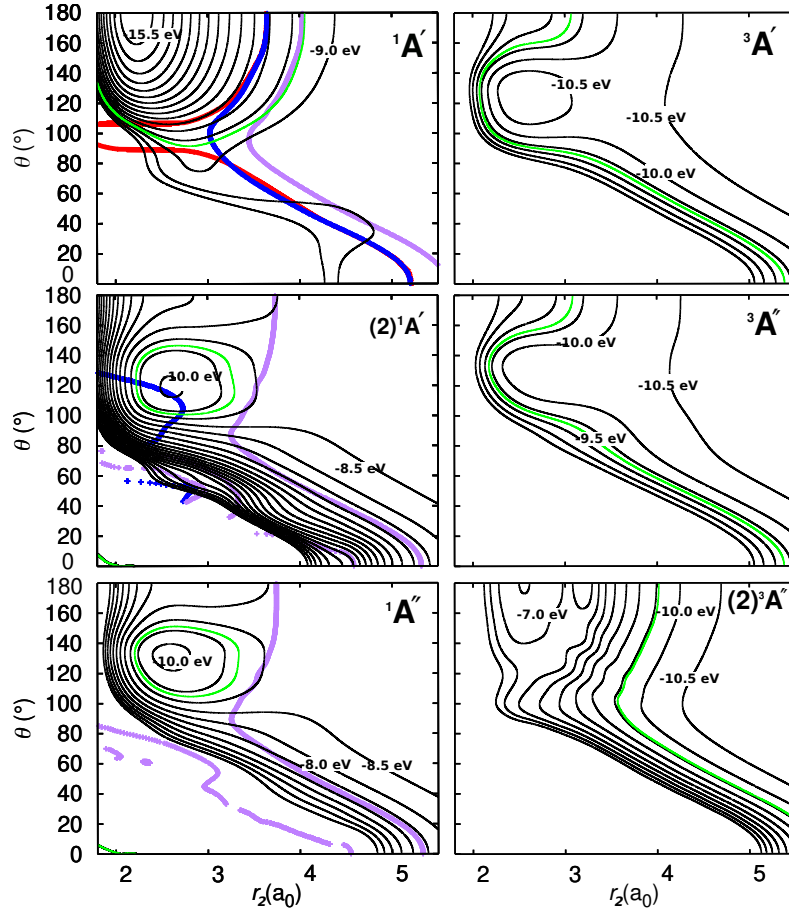


Figure S13: Crossings between the singlet and triplet PESs at the inner turning point ( $r_1 = 2.06 a_0$ ) of the CO diatom. The distance  $r_2$  is the second CO distance. Contour representation of the singlet (left) and triplet (right) states. Colour lines represent the intersection seam between the singlet and respective triplet surfaces.  ${}^1X-{}^3A'$  (red),  ${}^1X-{}^3A''$  (blue) and  ${}^1X-(2){}^3A''$  (magenta). Green line indicates a reference contour at  $-9.5$  eV relative to the  $O+O+C$  dissociation.

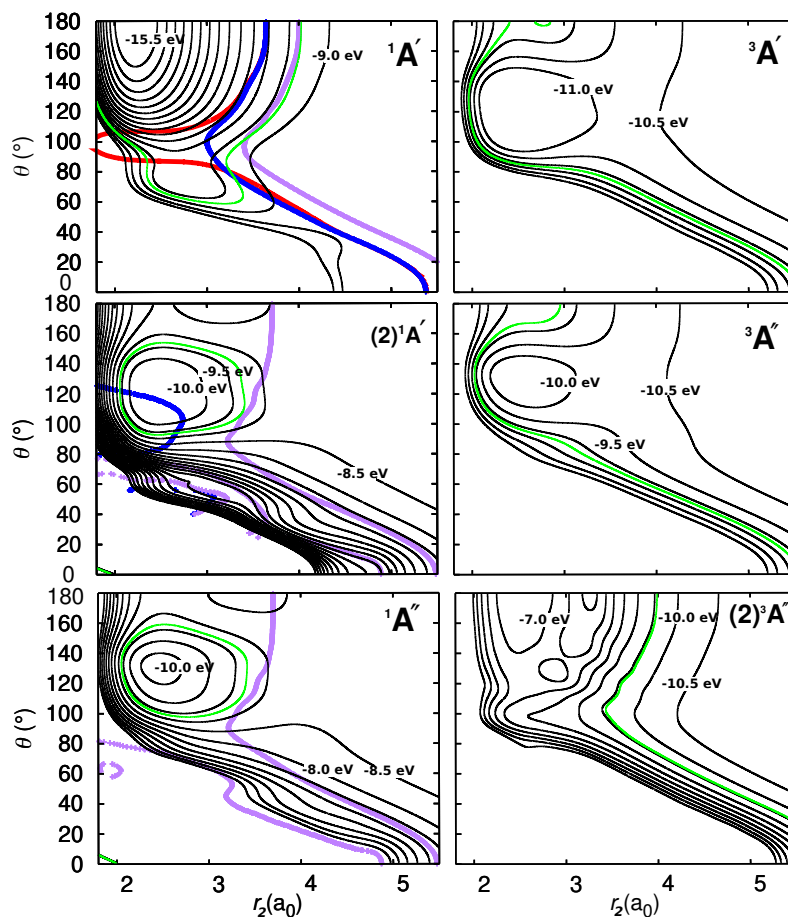


Figure S14: Crossings between the PESs at the outer turning point ( $r = 2.24 a_0$ ) of the CO diatom. The distance  $r_2$  is the second CO distance. Contour representation of the singlet (left) and triplet (right) states. Colour lines represent the intersection seam between the singlet and respective triplet surfaces.  $^1X-^3A'$  (red),  $^1X-^3A''$  (blue) and  $^1X-(2)^3A''$  (magenta). Green line indicates a reference contour at  $-9.5$  eV relative to the O+O+C dissociation.

Table S1: Rates for the  $C(^3P) + O_2(^3\Sigma_g^-) \rightarrow CO(^1\Sigma^+) + O(^1D_2)$  from 15 to 20000 K calculated using QCT on the  $^1A'$ ,  $(2)^1A'$ ,  $^1A''$  PESs. Units for rates are in  $\text{cm}^3\text{s}^{-1}\text{molecule}^{-1}$ .  $N_r$  is the number of reacting trajectories.

$T$ (K)	$N_r$	$k_1^f(^1A')$	$k_2^f((2)^1A')$	$k_3^f(^1A'')$	$k_1^f(^1A') + k_2^f((2)^1A') + k_3^f(^1A'')$
15	93057	$1.718 \times 10^{-10}$	0.000	0.000	$1.718 \times 10^{-10}$
27	90583	$1.245 \times 10^{-10}$	0.000	0.000	$1.245 \times 10^{-10}$
54	85791	$8.778 \times 10^{-11}$	0.000	0.000	$8.778 \times 10^{-11}$
63	84463	$8.261 \times 10^{-11}$	0.000	0.000	$8.261 \times 10^{-11}$
83	81512	$7.501 \times 10^{-11}$	0.000	0.000	$7.501 \times 10^{-11}$
112	77896	$6.868 \times 10^{-11}$	$2.617 \times 10^{-17}$	0.000	$6.868 \times 10^{-11}$
207	68861	$5.925 \times 10^{-11}$	$1.186 \times 10^{-14}$	0.000	$5.926 \times 10^{-11}$
295	66814	$5.551 \times 10^{-11}$	$7.371 \times 10^{-14}$	$2.095 \times 10^{-16}$	$5.558 \times 10^{-11}$
300	66493	$5.532 \times 10^{-11}$	$7.785 \times 10^{-14}$	$2.108 \times 10^{-16}$	$5.540 \times 10^{-11}$
500	58788	$5.152 \times 10^{-11}$	$5.265 \times 10^{-13}$	$6.183 \times 10^{-15}$	$5.205 \times 10^{-11}$
600	56358	$5.104 \times 10^{-11}$	$8.512 \times 10^{-13}$	$2.394 \times 10^{-14}$	$5.191 \times 10^{-11}$
1000	53536	$5.057 \times 10^{-11}$	$2.643 \times 10^{-12}$	$4.761 \times 10^{-13}$	$5.369 \times 10^{-11}$
1500	49748	$5.217 \times 10^{-11}$	$5.368 \times 10^{-12}$	$2.070 \times 10^{-12}$	$5.961 \times 10^{-11}$
2000	50708	$5.421 \times 10^{-11}$	$8.266 \times 10^{-12}$	$4.592 \times 10^{-12}$	$6.707 \times 10^{-11}$
2500	49341	$5.686 \times 10^{-11}$	$1.132 \times 10^{-11}$	$7.810 \times 10^{-12}$	$7.599 \times 10^{-11}$
3000	48425	$5.955 \times 10^{-11}$	$1.434 \times 10^{-11}$	$1.159 \times 10^{-11}$	$8.549 \times 10^{-11}$
4000	46964	$6.442 \times 10^{-11}$	$2.102 \times 10^{-11}$	$1.942 \times 10^{-11}$	$1.049 \times 10^{-10}$
5000	46270	$6.939 \times 10^{-11}$	$2.752 \times 10^{-11}$	$2.757 \times 10^{-11}$	$1.245 \times 10^{-10}$
8000	52737	$8.250 \times 10^{-11}$	$4.748 \times 10^{-11}$	$5.138 \times 10^{-11}$	$1.814 \times 10^{-10}$
10000	52363	$9.090 \times 10^{-11}$	$6.025 \times 10^{-11}$	$6.469 \times 10^{-11}$	$2.158 \times 10^{-10}$
12000	51930	$9.818 \times 10^{-11}$	$7.120 \times 10^{-11}$	$7.585 \times 10^{-11}$	$2.452 \times 10^{-10}$
15000	50987	$1.066 \times 10^{-10}$	$8.462 \times 10^{-11}$	$9.010 \times 10^{-11}$	$2.813 \times 10^{-10}$
20000	49054	$1.164 \times 10^{-10}$	$1.013 \times 10^{-10}$	$1.054 \times 10^{-10}$	$3.232 \times 10^{-10}$

Table S2: Rate coefficients for the  $\text{C}(^3\text{P}) + \text{O}_2(^3\Sigma_g^-) \rightarrow \text{CO}(^1\Sigma^+) + \text{O}(^3\text{P})$  from 15 to 20000 K calculated using QCT on the  $^3A'$  and  $^3A''$  PESs. Units are in  $\text{cm}^3\text{s}^{-1}\text{molecule}^{-1}$ .  $N_r$  is the number of reacting trajectories.

$T$ (K)	$N_r$	$k_1^f(^3A')$	$k_2^f(^3A'')$	$k_1^f(^3A') + k_2^f(^3A'')$
15	49736	$8.414 \times 10^{-11}$	0.000	$8.414 \times 10^{-11}$
27	47390	$5.682 \times 10^{-11}$	0.000	$5.682 \times 10^{-11}$
54	44900	$3.632 \times 10^{-11}$	0.000	$3.632 \times 10^{-11}$
63	44406	$3.337 \times 10^{-11}$	0.000	$3.337 \times 10^{-11}$
83	43644	$2.949 \times 10^{-11}$	0.000	$2.949 \times 10^{-11}$
112	43489	$2.671 \times 10^{-11}$	0.000	$2.671 \times 10^{-11}$
207	43238	$2.460 \times 10^{-11}$	0.000	$2.460 \times 10^{-11}$
295	46131	$2.486 \times 10^{-11}$	$1.467 \times 10^{-15}$	$2.487 \times 10^{-11}$
300	46187	$2.506 \times 10^{-11}$	$1.476 \times 10^{-15}$	$2.506 \times 10^{-11}$
500	46573	$2.742 \times 10^{-11}$	$8.043 \times 10^{-14}$	$2.750 \times 10^{-11}$
600	46856	$2.906 \times 10^{-11}$	$1.818 \times 10^{-13}$	$2.924 \times 10^{-11}$
1000	50249	$3.498 \times 10^{-11}$	$1.321 \times 10^{-12}$	$3.630 \times 10^{-11}$
1500	50968	$4.156 \times 10^{-11}$	$4.213 \times 10^{-12}$	$4.578 \times 10^{-11}$
2000	54396	$4.706 \times 10^{-11}$	$8.086 \times 10^{-12}$	$5.514 \times 10^{-11}$
3000	54474	$5.717 \times 10^{-11}$	$1.729 \times 10^{-11}$	$7.446 \times 10^{-11}$
4000	54387	$6.554 \times 10^{-11}$	$2.710 \times 10^{-11}$	$9.264 \times 10^{-11}$
5000	54311	$7.304 \times 10^{-11}$	$3.655 \times 10^{-11}$	$1.096 \times 10^{-10}$
8000	62916	$9.208 \times 10^{-11}$	$6.297 \times 10^{-11}$	$1.551 \times 10^{-10}$
10000	62254	$1.025 \times 10^{-10}$	$7.745 \times 10^{-11}$	$1.799 \times 10^{-10}$
12000	61260	$1.113 \times 10^{-10}$	$8.944 \times 10^{-11}$	$2.007 \times 10^{-10}$
15000	59333	$1.205 \times 10^{-10}$	$1.027 \times 10^{-10}$	$2.232 \times 10^{-10}$
20000	55854	$1.306 \times 10^{-10}$	$1.166 \times 10^{-10}$	$2.472 \times 10^{-10}$

Table S3: Rate coefficients for the  $\text{CO}(^1\Sigma^+) + \text{O}(^1\text{D}) \rightarrow \text{C}(^3\text{P}) + \text{O}_2(^3\Sigma_g^-)$  from 3000 to 20000 K calculated using QCT on the  $^1A'$ ,  $(2)^1A'$ ,  $^1A''$  PESs. Units are in  $\text{cm}^3\text{s}^{-1}\text{molecule}^{-1}$ .  $N_r$  is the number of reacting trajectories.

$T$ (K)	$N_r$	$k_1^r(^1A')$	$k_2^r((2)^1A')$	$k_3^r(^1A'')$	$k_1^r(^1A') + k_2^r((2)^1A') + k_3^r(^1A'')$
3000	0	0.000	0.000	0.000	0.000
4000	3	$6.226 \times 10^{-16}$	$3.738 \times 10^{-16}$	0.000	$9.964 \times 10^{-16}$
5000	16	$6.236 \times 10^{-15}$	$3.239 \times 10^{-15}$	$4.351 \times 10^{-15}$	$1.383 \times 10^{-14}$
8000	383	$2.902 \times 10^{-13}$	$1.588 \times 10^{-13}$	$1.651 \times 10^{-13}$	$6.141 \times 10^{-13}$
10000	1037	$9.278 \times 10^{-13}$	$5.759 \times 10^{-13}$	$6.744 \times 10^{-13}$	$2.178 \times 10^{-12}$
12000	1897	$1.928 \times 10^{-12}$	$1.533 \times 10^{-12}$	$1.653 \times 10^{-12}$	$5.114 \times 10^{-12}$
15000	3711	$4.616 \times 10^{-12}$	$3.796 \times 10^{-12}$	$4.239 \times 10^{-12}$	$1.265 \times 10^{-11}$
20000	6655	$1.008 \times 10^{-11}$	$8.983 \times 10^{-12}$	$9.373 \times 10^{-12}$	$2.844 \times 10^{-11}$

Table S4: Rate coefficients for the  $\text{CO}(^1\Sigma^+) + \text{O}(^3\text{P}) \rightarrow \text{C}(^3\text{P}) + \text{O}_2(^3\Sigma_g^-)$  from 3000 to 20000 K calculated using QCT on the  $^3A'$  and  $^3A''$  PESs. Units are in  $\text{cm}^3\text{s}^{-1}\text{molecule}^{-1}$ .  $N_r$  is the number of reacting trajectories.

$T$ (K)	$N_r$	$k_1^r(^3A')$	$k_2^r(^3A'')$	$k_1^r(^3A') + k_2^r(^3A'')$
3000	0	0.000	0.000	0.000
4000	0	0.000	0.000	0.000
5000	2	$9.055 \times 10^{-17}$	$2.175 \times 10^{-17}$	$1.123 \times 10^{-16}$
8000	223	$1.429 \times 10^{-14}$	$7.940 \times 10^{-15}$	$2.223 \times 10^{-14}$
10000	1332	$9.277 \times 10^{-14}$	$6.892 \times 10^{-14}$	$1.617 \times 10^{-13}$
12000	4339	$3.340 \times 10^{-13}$	$2.609 \times 10^{-13}$	$5.948 \times 10^{-13}$
15000	11796	$1.098 \times 10^{-12}$	$9.348 \times 10^{-13}$	$2.033 \times 10^{-12}$
20000	28176	$3.449 \times 10^{-12}$	$3.087 \times 10^{-12}$	$6.535 \times 10^{-12}$

Table S5: Temperature dependent rates for the  $\text{CO}_A(^1\Sigma^+) + \text{O}_B(^3\text{P}) \rightarrow \text{CO}_B(^1\Sigma^+) + \text{O}_A(^3\text{P})$  exchange reaction from 500 to 20000 K calculated using QCT on the  $^3A'$  PESs. Units are in  $\text{cm}^3\text{s}^{-1}\text{molecule}^{-1}$ .  $N_r$  is the number of reacting trajectories.

$T$ (K)	$N$	$k_1^f(^3A')$	$k_1^f(^3A'')$	$k_1^f(^3A' + ^3A'')$	$\Delta k_1^f(^3A' + ^3A'')$
500	57	$3.859 \times 10^{-16}$	$1.053 \times 10^{-16}$	$4.912 \times 10^{-16}$	$3.052 \times 10^{-16}$
1000	425	$3.511 \times 10^{-14}$	$1.242 \times 10^{-14}$	$4.754 \times 10^{-14}$	$1.972 \times 10^{-15}$
2000	4734	$5.570 \times 10^{-13}$	$2.812 \times 10^{-13}$	$8.382 \times 10^{-13}$	$1.746 \times 10^{-14}$
3000	11621	$1.503 \times 10^{-12}$	$9.694 \times 10^{-13}$	$2.472 \times 10^{-12}$	$3.340 \times 10^{-14}$
4000	20393	$2.649 \times 10^{-12}$	$2.012 \times 10^{-12}$	$4.661 \times 10^{-12}$	$3.969 \times 10^{-14}$
5000	28143	$3.808 \times 10^{-12}$	$3.233 \times 10^{-12}$	$7.041 \times 10^{-12}$	$5.890 \times 10^{-14}$
8000	52280	$7.947 \times 10^{-12}$	$7.777 \times 10^{-12}$	$1.572 \times 10^{-11}$	$7.493 \times 10^{-14}$
10000	78807	$1.116 \times 10^{-11}$	$1.099 \times 10^{-11}$	$2.215 \times 10^{-11}$	$1.088 \times 10^{-13}$
12000	93891	$1.459 \times 10^{-11}$	$1.468 \times 10^{-11}$	$2.927 \times 10^{-11}$	$1.606 \times 10^{-13}$
15000	127016	$2.008 \times 10^{-11}$	$2.043 \times 10^{-11}$	$4.051 \times 10^{-11}$	$3.037 \times 10^{-13}$
20000	182669	$2.932 \times 10^{-11}$	$3.001 \times 10^{-11}$	$5.933 \times 10^{-11}$	$1.990 \times 10^{-13}$

Table S6: Rate coefficients for the  $\text{CO}(^1\Sigma^+) + \text{O}(^3\text{P}) \rightarrow \text{CO}(^1\Sigma^+) + \text{O}(^3\text{P})$  vibrational relaxation  $\nu = 1 \rightarrow 0$  from 300 to 5000 K calculated using QCT on the  $^3A'$  and  $^3A''$  PESs. Units for rates are in  $\text{cm}^3\text{s}^{-1}\text{molecule}^{-1}$  and  $N_r$  is the number of reacting trajectories.

$T$ (K)	$N_r$	$k_1^f(^3A')$	$k_1^f(^3A'')$	$k_1^f(^3A') + k_1^f(^3A'')$
300	0	0.000	0.000	0.000
500	5	$1.086 \times 10^{-15}$	$9.675 \times 10^{-16}$	$3.021 \times 10^{-15}$
1000	301	$1.235 \times 10^{-13}$	$1.081 \times 10^{-13}$	$3.396 \times 10^{-13}$
2000	1713	$1.329 \times 10^{-12}$	$1.490 \times 10^{-12}$	$4.309 \times 10^{-12}$
3000	2956	$3.043 \times 10^{-12}$	$3.966 \times 10^{-12}$	$1.097 \times 10^{-11}$
4000	3950	$4.780 \times 10^{-12}$	$6.701 \times 10^{-12}$	$1.818 \times 10^{-11}$
5000	4524	$6.237 \times 10^{-12}$	$9.933 \times 10^{-12}$	$2.610 \times 10^{-11}$